

Optimal control of Bose–Einstein condensates in three dimensions

This content has been downloaded from IOPscience. Please scroll down to see the full text.

2015 New J. Phys. 17 113027

(<http://iopscience.iop.org/1367-2630/17/11/113027>)

View [the table of contents for this issue](#), or go to the [journal homepage](#) for more

Download details:

IP Address: 129.187.254.46

This content was downloaded on 17/02/2017 at 06:58

Please note that [terms and conditions apply](#).

You may also be interested in:

[Vibrational state inversion of a Bose--Einstein condensate: optimal control and state tomography](#)

Robert Bücke, Tarik Berrada, Sandrine van Frank et al.

[Spatial adiabatic passage: a review of recent progress](#)

R Menchon-Enrich, A Benseny, V Ahufinger et al.

[Controlling the transport of an ion: classical and quantum mechanical solutions](#)

H A Fürst, M H Goerz, U G Poschinger et al.

[Beyond mean-field dynamics of ultra-cold bosonic atoms in higher dimensions: facing the challenges with a multi-configurational approach](#)

V J Bolsinger, S Krönke and P Schmelcher

[Engineering dark solitary waves in ring-trap Bose–Einstein condensates](#)

D Gallucci and N P Proukakis

[Rydberg dressing: understanding of collective many-body effects and implications for experiments](#)

J B Balewski, A T Krupp, A Gaj et al.

[The instanton method and its numerical implementation in fluid mechanics](#)

Tobias Grafke, Rainer Grauer and Tobias Schäfer

[Quantum control problems with H1 cost](#)

G von Winckel and A Borzi

[Microwave-dressed state-selective potentials for atom interferometry](#)

V Guarrera, R Szmuk, J Reichel et al.



PAPER

Optimal control of Bose–Einstein condensates in three dimensions

OPEN ACCESS

RECEIVED
5 August 2015REVISED
22 September 2015ACCEPTED FOR PUBLICATION
12 October 2015PUBLISHED
9 November 2015

Content from this work
may be used under the
terms of the [Creative
Commons Attribution 3.0
licence](#).

Any further distribution of
this work must maintain
attribution to the
author(s) and the title of
the work, journal citation
and DOI.

J-F Mennemann^{1,3}, D Matthes², R-M Weishäupl³ and T Langen^{4,5}¹ Automation and Control Institute, Complex Dynamical Systems Group, Vienna University of Technology, Gusshausstrasse 27–29, A-1040 Vienna, Austria² Zentrum Mathematik, Technische Universität München, D-85747 Garching, Germany³ Department of Mathematics, University of Vienna, A-1090 Vienna, Austria⁴ Vienna Center for Quantum Science and Technology, Atominstytut, TU Wien, Stadionallee 2, A-1020 Vienna, Austria⁵ JILA, University of Colorado and NIST, Boulder, CO 80309, USAE-mail: mennemann@acin.tuwien.ac.at and tim.langen@colorado.edu**Keywords:** ultracold quantum gases, optimal control theory, atomtronics, Gross–Pitaevskii equation, Bose–Einstein condensates, numerical methodsSupplementary material for this article is available [online](#)**Abstract**

Ultracold gases promise many applications in quantum metrology, simulation and computation. In this context, optimal control theory (OCT) provides a versatile framework for the efficient preparation of complex quantum states. However, due to the high computational cost, OCT of ultracold gases has so far mostly been applied to one-dimensional (1D) problems. Here, we realize computationally efficient OCT of the Gross–Pitaevskii equation to manipulate Bose–Einstein condensates in all three spatial dimensions. We study various realistic experimental applications where 1D simulations can only be applied approximately or not at all. Moreover, we provide a stringent mathematical footing for our scheme and carefully study the creation of elementary excitations and their minimization using multiple control parameters. The results are directly applicable to recent experiments and might thus be of immediate use in the ongoing effort to employ the properties of the quantum world for technological applications.

1. Introduction

Over the last decade, the ever increasing experimental toolbox of atomic, optical and molecular physics has led to an exciting improvement in the control and understanding of complex quantum systems [1]. Recently, this has resulted in an important shift of paradigm. While quantum systems were previously mostly studied to check the validity of theoretical models, interest has now increased in their manipulation for specific technological applications. Prototypical examples for this shift of paradigm are atomic interferometers for quantum enhanced metrology [2–4], atomic field probes [5] and microscopes [6, 7], inertial sensors [8], atomic clocks [9], or applications in quantum computing [10, 11] and quantum simulation [12].

In many cases, these applications rely on the controlled preparation of a well-defined quantum many-body state with particular properties. One of the key experimental challenges is thus the efficient transfer of a system to such a state. Optimal control theory (OCT) is a mathematical tool to devise control strategies for this transfer [13]. It is well studied in many physical systems, ranging from atoms and molecules to solid-state systems [14–18].

In this work, we apply it to the control of a dilute atomic Bose–Einstein condensate (BEC), a system which is well described by the three-dimensional (3D) Gross–Pitaevskii equation (GPE) [19, 20]. Such BECs form a versatile experimental platform for the storage, manipulation and probing of interacting quantum fields with high precision [1]. In a seminal work Hohenester *et al* [21] demonstrated that OCT [22] provides a highly efficient way to realize the transfer of a BEC to a target state, vastly outperforming more simple schemes. In this context, it has also been shown that OCT is robust against fluctuations and decoherence, and can also specifically

take into account experimental constraints [23]. This has recently led to first experimental demonstrations [24, 25].

OCT of BECs has so far been mostly used in one-dimensional (1D) settings, as the number of necessary spatial discretization points and hence the numerical costs scale exponentially with the number of dimensions. [26]. However, most experimental situations can only approximately be described by a 1D model, which has so far limited the applicability of OCT to real-life situations.

In the following we demonstrate the first OCT of a BEC in all three spatial dimensions and study the physical insights that come with this advance. As we demonstrate through a number of examples, extending optimal control of BECs from 1D to 3D is the crucial step to bridge the gap from limited proof-of-principle experiments to a general applicability of this powerful technique. For example, we show how collective excitations are inevitably created as a result of the control. These excitations are directly connected to the nonlinear nature of the GPE and can only be fully captured and minimized in a 3D treatment including multiple control parameters.

Finally, we provide a detailed description of all necessary numerical details to make our work the starting point for the application of the presented technique in many future experiments.

2. The control problem

We start with a brief review of OCT, as well as of the description of BECs in terms of the GPE.

2.1. Gross–Pitaevskii equation

The mean-field dynamics of a BEC is described by the GPE

$$i\hbar\partial_t\psi = -\frac{\hbar^2}{2m}\Delta\psi + V_\lambda\psi + g|\psi|^2\psi, \quad (1)$$

where $\psi \equiv \psi(\mathbf{r}, t)$ denotes a complex-valued wave function, with initial condition $\psi(\mathbf{r}, 0) \equiv \psi_0 \in L^2(\mathbb{R}^3; \mathbb{C})$. Here, $V_\lambda \equiv V(\mathbf{r}, \boldsymbol{\lambda}(t))$ is an external potential that is characterized by a single or several control parameters denoted by the vector $\boldsymbol{\lambda}$. Assuming that the wave function is normalized to unity, the coupling constant $g = N4\pi\hbar^2a_s m^{-1}$ is defined by the mass m , the s -wave scattering length a_s and the number N of atoms in the BEC. For example, for ultracold gases of ^{87}Rb atoms, the atomic mass is given by $m = 1.44 \times 10^{-25}$ kg and the s -wave scattering length by $a_s = 5.24$ nm. Measuring length in units of $l_0 = 1 \times \mu\text{m}$, mass in units of the atomic mass and time in units of $t_0 = ml_0^2/\hbar$, equation (1) can be written as

$$i\partial_t\psi = -\frac{1}{2}\Delta\psi + V_\lambda\psi + g|\psi|^2\psi \quad (2)$$

which is the starting point for our considerations below.

2.2. Optimal control problem

We seek to find an optimal time-evolution of the m -component control parameter

$$\boldsymbol{\lambda} : (0, T) \rightarrow \mathbb{R}^m, \quad \boldsymbol{\lambda}(0) = \boldsymbol{\lambda}_0, \quad \boldsymbol{\lambda}(T) = \boldsymbol{\lambda}_T,$$

which steers the system from the initial state ψ_0 at time zero to a desired state ψ_d at final time T . Without loss of generality we assume that ψ_0 and ψ_d are ground state solutions of the stationary GPE corresponding to the smooth external potentials $V_{\boldsymbol{\lambda}_0}$ and $V_{\boldsymbol{\lambda}_T}$ at times $t = 0$ and $t = T$, respectively, with fixed parameters $\boldsymbol{\lambda}_0, \boldsymbol{\lambda}_T$. To find the time evolution we apply well-known techniques from OCT [21]. As cost functional, we use

$$J(\boldsymbol{\lambda}, \psi) = \frac{1}{2} \left(1 - \left| \langle \psi_d, \psi(T) \rangle \right|^2 \right) + \frac{\gamma}{2} \int_0^T \left| \partial_t \boldsymbol{\lambda}(t) \right|^2 dt, \quad (3)$$

where $\langle u, v \rangle = \int_{\mathbb{R}^3} u(\mathbf{r})^* v(\mathbf{r}) d\mathbf{r}$ denotes the standard scalar product of $u, v \in L^2(\mathbb{R}^3; \mathbb{C})$. The definition (3) is the generalization of the functional used in [21, 23, 26–30] to a multi-component control parameter $\boldsymbol{\lambda}$. The first term in J measures the proximity of ψ to the desired state ψ_d at the end of the steering process. The expression $\widetilde{\mathcal{F}}(\psi) = 1 - |\langle \psi_d, \psi \rangle|^2$ is known as the infidelity and provides a measure for the difference of ψ and ψ_d . In detail, it quantifies the L^2 -norm of ψ 's component that is orthogonal to ψ_d . The second term regularizes the control trajectory to account for the fact that parameters can never be changed infinitely fast in a real experiment. Here, $\gamma > 0$ sets the penalty for fast variations of $\boldsymbol{\lambda}(t)$. For our examples below we find that already a very small value $\gamma = 1 \times 10^{-6}$ yields a satisfactory regularization.

Our goal is to minimize $J(\boldsymbol{\lambda}, \psi)$ subject to the constraint that ψ solves the GPE (equation (2)) with the initial condition given by the respective ψ_0 . To this end, one introduces the Lagrange function

$$L(\boldsymbol{\lambda}, \psi, p) = J(\boldsymbol{\lambda}, \psi) + \operatorname{Re} \int_0^T \int_{\mathbb{R}^3} p^* \left(i\partial_t \psi + \frac{1}{2} \Delta \psi - V_\lambda \psi - g |\psi|^2 \psi \right) dt d\mathbf{r} \quad (4)$$

where $p(\mathbf{r}, t)$ acts as a generalized Lagrange multiplier [22]. At a local minimum $(\boldsymbol{\lambda}, \psi, p)$ of J , all three variational derivatives $D_p L(\boldsymbol{\lambda}, \psi, p)[\delta p]$, $D_\psi L(\boldsymbol{\lambda}, \psi, p)[\delta \psi]$ and $D_\lambda L(\boldsymbol{\lambda}, \psi, p)[\delta \boldsymbol{\lambda}]$ vanish for all admissible variations δp , $\delta \psi$ and $\delta \boldsymbol{\lambda}$, respectively. The corresponding three conditions constitute the optimality system

$$i\partial_t \psi = -\frac{1}{2} \Delta \psi + V_\lambda \psi + g |\psi|^2 \psi, \quad (5a)$$

$$i\partial_t p = -\frac{1}{2} \Delta p + V_\lambda p + 2g |\psi|^2 p + g \psi^2 p^*, \quad (5b)$$

$$\gamma \frac{d^2}{dt^2} \boldsymbol{\lambda} = -\operatorname{Re} \left\langle \psi, \left(\partial_\lambda V_\lambda \right) p \right\rangle, \quad (5c)$$

together with the initial and terminal conditions

$$\psi(0) = \psi_0, \quad (6a)$$

$$ip(T) = -\left\langle \psi_d, \psi(T) \right\rangle \psi_d, \quad (6b)$$

$$\boldsymbol{\lambda}(0) = \boldsymbol{\lambda}_0, \quad \boldsymbol{\lambda}(T) = \boldsymbol{\lambda}_T. \quad (6c)$$

In general, no analytical solutions are available for (5) with (6). Here we use an iterative method to find a numerical approximation of the solution. For this purpose it is useful to introduce the reduced cost functional

$$\hat{J}(\boldsymbol{\lambda}) = J(\boldsymbol{\lambda}, \psi_\lambda), \quad (7)$$

where ψ_λ denotes the unique solution of the GPE for a given control parameter curve $\boldsymbol{\lambda}$. The goal is to find a local (or, preferably, even global) minimizer $\boldsymbol{\lambda}^*$ of \hat{J} .

The most straight-forward iterative procedure that can be employed is the method of steepest descent,

$$\boldsymbol{\lambda}^{k+1} = \boldsymbol{\lambda}^k - \alpha^k \nabla \hat{J}(\boldsymbol{\lambda}^k), \quad k = 0, 1, 2, \dots \quad (8)$$

To determine an appropriate step size α^k , we perform a line search in each iteration:

$$\alpha^k = \arg \min_{\alpha} \hat{J}(\boldsymbol{\lambda}^k - \alpha \nabla \hat{J}(\boldsymbol{\lambda}^k)). \quad (9)$$

Here the upper index denotes the iteration step. A comment is due on the use of the gradient $\nabla \hat{J}(\boldsymbol{\lambda}^k)$ in (8). Recall that the gradient of \hat{J} at $\boldsymbol{\lambda}$ with respect to a specific inner product $(\cdot, \cdot)_X$ on the space X of admissible variations $\delta \boldsymbol{\lambda}$ is the uniquely determined element $\nabla \hat{J} \in X$ such that $(\nabla \hat{J}, \delta \boldsymbol{\lambda})_X = D_\lambda \hat{J}(\boldsymbol{\lambda})[\delta \boldsymbol{\lambda}]$ for all admissible variations $\delta \boldsymbol{\lambda} \in X$. The gradient thus depends sensitively on the choice of the inner product $(\cdot, \cdot)_X$ on X . It has been pointed out already in [27] that any admissible variation $\delta \boldsymbol{\lambda}$ must have a finite value in the penalty term, i.e., its weak time derivative $\partial_t \delta \boldsymbol{\lambda}$ must be square-integrable on $(0, T)$, and must respect the boundary conditions in (6c), i.e., $\delta \boldsymbol{\lambda}(0) = \delta \boldsymbol{\lambda}(T) = 0$. A natural choice for $(\cdot, \cdot)_X$ is thus the $H_0^1(0, T, \mathbb{R}^m)$ -scalar product,

$$(\mathbf{u}, \mathbf{v}) := \int_0^T \partial_t \mathbf{u}(t) \cdot \partial_t \mathbf{v}(t) dt. \quad (10)$$

A calculation, which we present in the appendix, shows that this choice of $(\cdot, \cdot)_X$ yields

$$\frac{d^2}{dt^2} [\nabla \hat{J}(\boldsymbol{\lambda})] = \gamma \ddot{\boldsymbol{\lambda}} + \operatorname{Re} \left\langle \psi, \left(\partial_\lambda V_\lambda \right) p \right\rangle, \quad (11a)$$

$$[\nabla \hat{J}(\boldsymbol{\lambda})](0) = \mathbf{0}, \quad (11b)$$

$$[\nabla \hat{J}(\boldsymbol{\lambda})](T) = \mathbf{0}, \quad (11c)$$

wherein ψ and p are solutions of (5a) and (6a) or (5b) and (6b), respectively. By definition, $\nabla \hat{J}$ vanishes at the boundaries $t = 0$ and $t = T$, and so the iteration (8) preserves the boundary conditions (6c). We emphasize that the seemingly canonical choice of $(\cdot, \cdot)_X$ as the standard L^2 -scalar product would not allow to specify boundary data for $\nabla \hat{J}$, which would result in a severe loss of stability of the optimization algorithm.

2.3. Implementation

In the situations considered below we found that the method of steepest descent (see equation (8)) works reliably. However, using more advanced methods the number of iterations needed to ensure convergence of the algorithm can be reduced significantly. In fact, our solver is based on the nonlinear conjugate gradient scheme of Hager and Zhang [31], which has also been employed in [27] for optimal control of the 1D GPE. We stress that

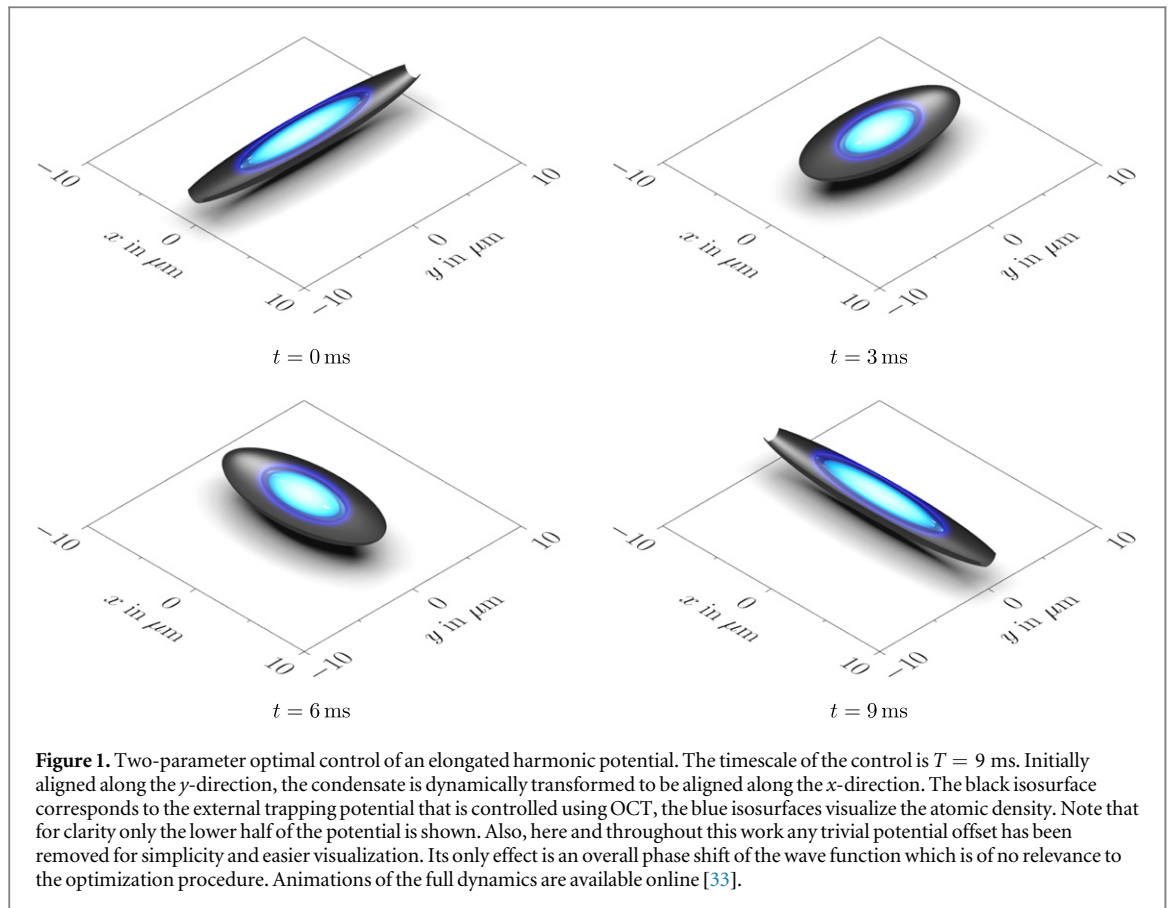


Figure 1. Two-parameter optimal control of an elongated harmonic potential. The timescale of the control is $T = 9$ ms. Initially aligned along the y -direction, the condensate is dynamically transformed to be aligned along the x -direction. The black isosurface corresponds to the external trapping potential that is controlled using OCT, the blue isosurfaces visualize the atomic density. Note that for clarity only the lower half of the potential is shown. Also, here and throughout this work any trivial potential offset has been removed for simplicity and easier visualization. Its only effect is an overall phase shift of the wave function which is of no relevance to the optimization procedure. Animations of the full dynamics are available online [33].

all inner products and norms related to the nonlinear conjugate gradient scheme need to be expressed in terms of the inner product given in equation (10).

The reduced cost functional (7) needs to be evaluated several times per iteration. Moreover, at the beginning of each iteration a gradient vector needs to be determined using equation (11a). Solutions to the time-dependent GPE (5a) and the adjoint equation (5b) are obtained via the time-splitting spectral method [32]. Initial and desired final states for a given potential are found by imaginary time propagation.

In order to accelerate the solving of the optimal control problem we perform all computations on the graphics processing unit (GPU) of a powerful graphics card. To speed up the calculations and ensure convergence of the algorithm we start each optimization with a coarse spatial grid and a relatively big time step Δt . The result for λ is used as an input for another round of optimization on a finer grid. This procedure is repeated until the algorithm converges to a final time-evolution for λ . A detailed description of our implementation is given in the appendix.

3. Examples

In the following we demonstrate the results of our scheme by considering three applications of increasing complexity, which are directly connected to recent experiments.

3.1. Harmonic oscillator potential

In the first application we study a BEC in an elongated harmonic potential. Initially, the trap frequencies are chosen such that the condensate is aligned along the y direction. Using a suitable time-evolution of the trap frequencies, we aim to rotate the condensate by $\pi/2$, while keeping it in the ground state of the external potential.

An example of the transition is visualized in figure 1. It can be understood as a toy example of a broad class of experimental protocols in which the trapping geometry is changed, e.g. to mode match different traps [34], to (de)compress a trap [35], to load an optical lattice [36] or to transfer condensates into dynamical potentials for atomtronics [37, 38]. Conceptually similar pulsed manipulations are also performed to focus BECs in time-of-flight expansion [39].

3.1.1. Trapping potential

The harmonic potential in this example is given by

$$V_{\lambda}(x, y, z) = \frac{m}{2} \left(\left[\omega_x(\lambda_1) \right]^2 x^2 + \left[\omega_y(\lambda_2) \right]^2 y^2 + \omega_z^2 z^2 \right),$$

wherein the frequencies ω_x and ω_y can be set independently via the control parameters λ_1 and λ_2 . More precisely, we transform the external potential from an initial configuration with $\omega_x = \omega_x^i$ and $\omega_y = \omega_y^i$ at time $t = 0$ to a final configuration with $\omega_x = \omega_x^f$ and $\omega_y = \omega_y^f$ at the final time $t = T$. To this end, we parametrize ω_x and ω_y as

$$\begin{aligned} \omega_x(\lambda_1) &= \omega_x^i + \lambda_1(\omega_x^f - \omega_x^i), \\ \omega_y(\lambda_2) &= \omega_y^i + \lambda_2(\omega_y^f - \omega_y^i), \end{aligned}$$

with

$$\begin{aligned} \lambda_1(0) &= 0, & \lambda_1(T) &= 1, \\ \lambda_2(0) &= 0, & \lambda_2(T) &= 1. \end{aligned}$$

We note that these parametrizations, as all others discussed below, are chosen as an example and can easily be adjusted to the parameters accessible in a specific experimental realization.

3.1.2. Numerical simulations

In the following simulations the number of atoms is $N = 5000$, the final time is set to $T = 9$ ms and $\omega_z = 5$ kHz. The initial configuration of the trapping potential is given by $\omega_x^i = 5$ kHz and $\omega_y^i = 0.75$ kHz, the final configuration by $\omega_x^f = 0.75$ kHz and $\omega_y^f = 5$ kHz.

Before we discuss the result of the optimal control algorithm we first consider a numerical simulation as a benchmark, in which the control parameters λ_1 and λ_2 are varied linearly. The corresponding time-evolution of the trap frequencies ω_x and ω_y is depicted in figure 2(a).

In order to investigate the overlap of ψ with ψ_d beyond the end of the control we continue the time-evolution with $\lambda(t) = \lambda(T)$ for $t > T$. We proceed analogously in the other examples. As can be seen from figure 2(b) the infidelity decreases only slightly until $t = T$ and shows a strong oscillation for $t > T$. This behavior of the infidelity indicates that the final state differs significantly from the desired state ψ_d . This is also strikingly visualized by example snapshots of the density at time $t^* = 22$ ms in figures 2(c)–(e).

Next, we consider the result of the optimal control algorithm. Using $\lambda^0(t) = [0.25 \sin(\pi t/T) + t/T, -0.25 \sin(\pi t/T) + t/T]$ for $t \in [0, T]$ as a starting point, the algorithm converges to a solution that reduces the cost functional by four orders of magnitude. The time-evolution of the frequencies ω_x and ω_y is shown in figure 2(f), the time-evolution of the corresponding infidelity in figure 2(g). It can clearly be seen that the infidelity strongly decreases until the end of the control at $t = T$. Moreover, the infidelity remains on a very low level for $t > T$, indicating that the desired final state has been reached with high precision. Consequently, the deviations of the density to the density of the desired state at time $t = t^*$ are very close to zero as can be seen from figures 2(h)–(j). We note at this point that the evolution of the 3D wave functions can naturally only be described here in limited detail. A supplementary video that visualizes these dynamics in greater detail is available online [33].

3.2. Loading of a toroidal trap

In the second application we consider the loading of a toroidal trap as shown in figure 3. Such toroidal traps have recently been employed to realize atomic analogues of electrical circuits to study superflow and hysteresis [40–44].

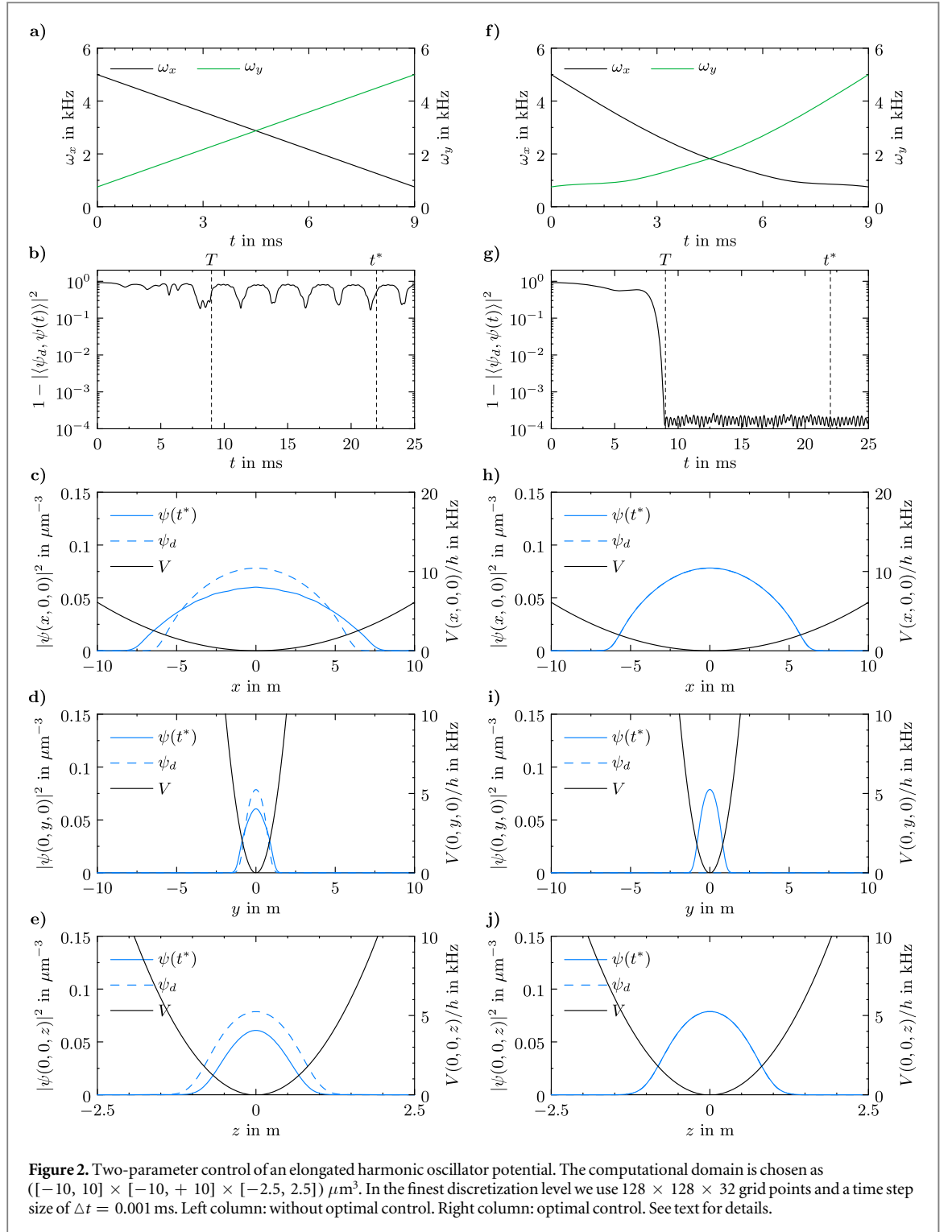
3.2.1. Trapping potential

The trapping potential is given by a slightly elongated harmonic potential and a Gaussian function centered at the origin of our coordinate system [40]

$$\begin{aligned} V_{\lambda}(x, y, z) &= \frac{m}{2} \left(\left[\omega_x(\lambda_1) \right]^2 x^2 + \omega_y^2 y^2 + \omega_z^2 z^2 \right) \\ &\quad + V_0(\lambda_2) \exp\left(-2(x^2 + y^2)/w_0^2\right). \end{aligned}$$

In an experiment this Gaussian function could for example correspond to a red-detuned laser beam realizing a repulsive dipole potential.

As illustrated in figure 3 we consider the transformation of the potential from an initial harmonic configuration with $\omega_x = \omega_x^i$ and $V_0 = 0$ at time $t = 0$ to a toroidal configuration with $\omega_x = \omega_x^f$ and $V_0 = V_0^*$ at the final time $t = T$. Hence, a suitable parameterization of ω_x and V_0 is given by



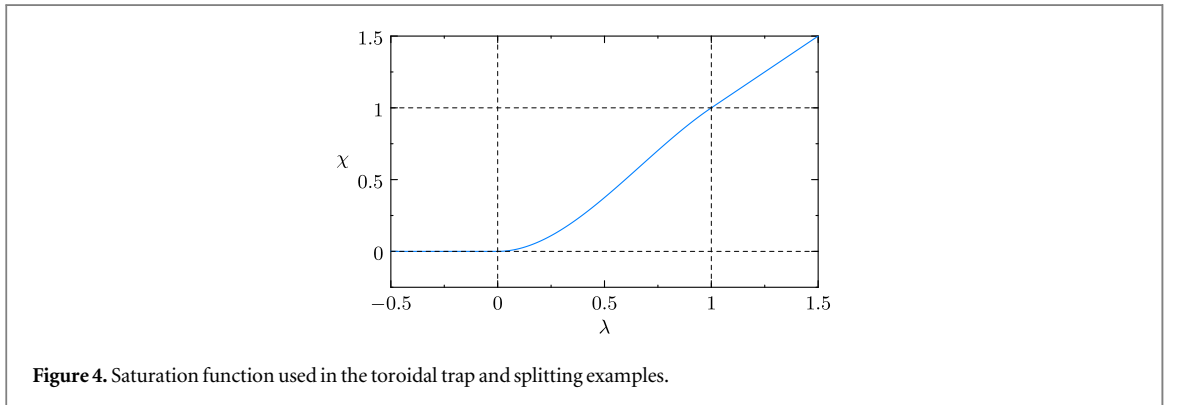
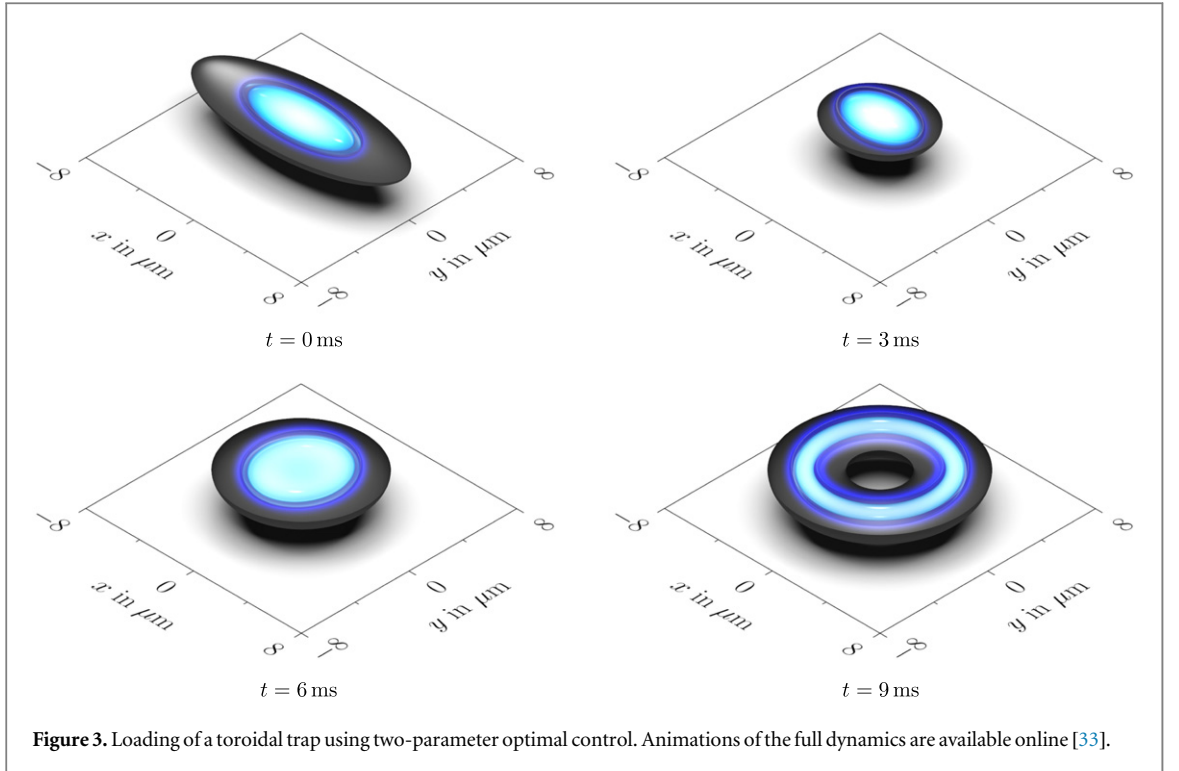
$$\omega_x(\lambda_1) = \omega_x^i + \lambda_1(\omega_x^f - \omega_x^i), \quad (12a)$$

$$V_0(\lambda_2) = V_0^* \chi(\lambda_2), \quad (12b)$$

where

$$\begin{aligned} \lambda_1(0) &= 0, & \lambda_1(T) &= 1, \\ \lambda_2(0) &= 0, & \lambda_2(T) &= 1. \end{aligned}$$

In equation (12b), χ plays the role of a saturation function. The use of the saturation function ensures that V_0 remains positive—and thus experimentally realizable—for any possible choice of λ_2 . This does not restrict the original control problem, as every experimentally realizable trajectory $V_0(t) \geq 0$ can be parametrized through a



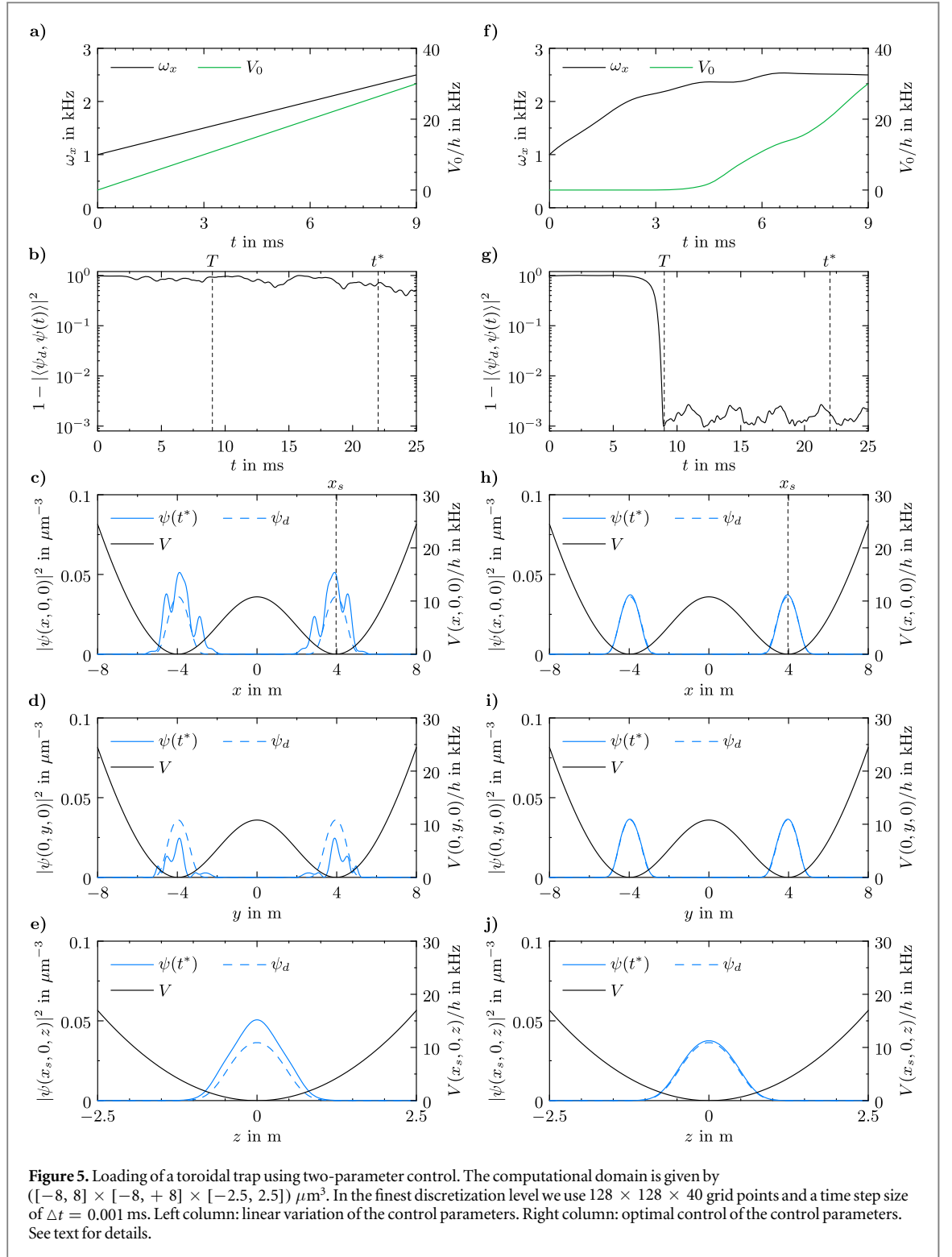
suitable $\lambda_2(t)$ in $V_0^* \chi(\lambda_2(t))$. In fact, we choose all parameters for the external potential to be close to previous experimental realizations. However, our approach also allows us to optimize more general situations where the parametrization of the trapping potential is more complicated [45].

Similar saturation functions are commonly used in control theory to realize limits on control parameters. In our particular case χ is implemented using a piecewise cubic hermite interpolating polynomial (PCHIP). Its functional form is shown in figure 4. The interpolating points are chosen such that χ always remains positive. Moreover, $\chi(0) = 0$ and $\chi(1) = 1$.

3.2.2. Numerical simulations

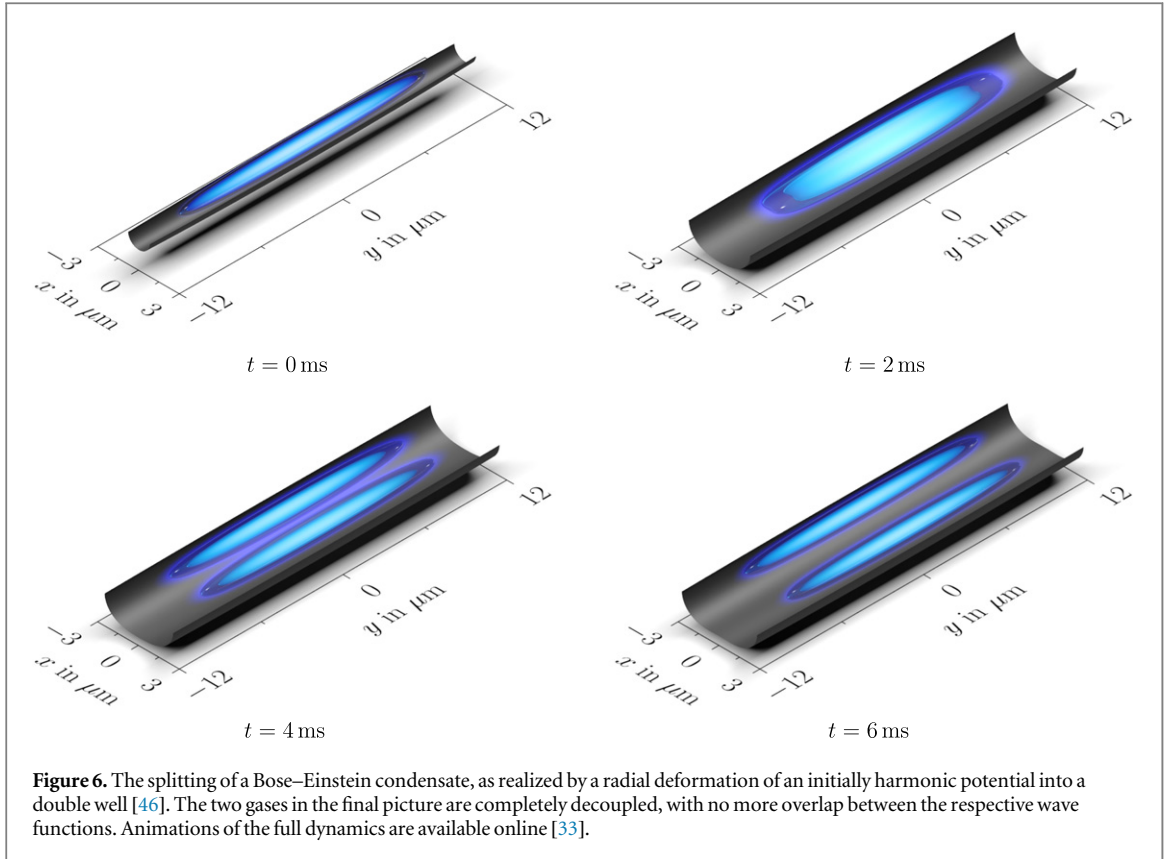
The following simulations are carried out using $V_0^* = h \times 30$ kHz, $w_0 = 5 \mu\text{m}$, $T = 9$ ms and $N = 5000$. The frequencies $\omega_y = 2.5$ kHz and $\omega_z = 5$ kHz are kept constant during the simulation. The initial configuration of the confinement potential is characterized by $\omega_x^i = 1$ kHz and $V_0(t=0)/h = 0$ kHz, whereas the final configuration is given by $\omega_x^f = 2.5$ kHz and $V_0(T)/h = V_0^*$.

As in the previous example we consider first the case where the parameters ω_x and V_0 are changed linearly (see figure 5(a)). Figure 5(b) reveals that the associated infidelity does not drop at all until $t = T$. For $t > T$ we observe a slight decrease of the infidelity. This can be attributed to the fact that, as time evolves, the density of the condensate becomes more evenly distributed in the toroidal trapping potential, bringing its wavefunction closer to ψ_d . However, as can be seen from figures 5(c)–(e), the final wave function still differs strongly from the wave function of the desired state after $t^* = 22$ ms.



Let us now discuss the result of the optimal control algorithm. An optimal time-evolution of the control parameters is given in figure 5(f). Intuitively this control can be understood as the result of two separate time-scales. During the first half of the control, the trap frequency ω_x is increased, while the limits imposed on λ_2 prohibit any change of V_0 . During the second half, on the other hand, V_0 is adjusted to its final value, while ω_x is only subject to small corrections.

Until the end of the control this leads to a drop in the infidelity by approximately three orders of magnitude, as visualized in figure 5(g). Furthermore, the infidelity remains bounded by 3×10^{-3} for $t > T$, which is well below the measurement sensitivity in typical experiments. Consequently, only slight deviations from the desired wavefunction at time $t^* = 22$ ms can be observed in figures 5(h)–(j).



3.3. Splitting

In terms of technological applications, a particular noteworthy realization of BECs is achieved using atom chips [47, 48]. On these chips micro-fabricated wires allow the precise manipulation of BECs using static, radio and microwave fields. As a third application we thus consider the splitting of a single condensate into two identical halves using such an atom chip [46]. A visualization is presented in figure 6. This splitting protocol has recently been used to study the non-equilibrium dynamics of quantum gases, revealing subtle effects, such as prethermalization [49–52], generalized statistical ensembles [53] and the light-cone-like emergence of thermal correlations [54, 55]. Moreover, it forms the basic building block for integrated matter-wave interferometers [56, 57].

3.3.1. Trapping potential

In the experiments the splitting is realized by dressing the static magnetic trapping potential with a strong near-field radio-frequency (RF) field. The unscaled static potential is given by $V_{\text{static}} = g_F \mu_B m_F |\mathbf{B}|$, with the magnetic field $\mathbf{B} = (B_x, B_y, B_z)$ being well approximated by the famous Ioffe–Pritchard form

$$\begin{aligned} B_x &= B_1 x - \frac{B_2}{2} xy, \\ B_z &= -B_1 z - \frac{B_2}{2} zy, \\ B_y &= B_0 + \frac{B_2}{2} \left[y^2 - \frac{1}{2}(x^2 + z^2) \right]. \end{aligned}$$

The parameters are given by $B_0 = \hbar\omega_0/m_F g_F \mu_B$, $B_1 = \sqrt{m\omega_\perp^2 B_0/m_F g_F \mu_B}$ and $B_2 = m\omega_\parallel^2/m_F g_F \mu_B$. In the following simulations we consider ^{87}Rb atoms which are trapped in the $5S_{1/2} F = 2$, $m_F = 2$ state where $g_F = 1/2$. The trap parameters are

$$\begin{aligned} \omega_0 &= 2\pi \times 390 \text{ kHz}, \\ \omega_x = \omega_z &\equiv \omega_\perp = 2\pi \times 2 \text{ kHz}, \\ \omega_y &\equiv \omega_\parallel = 2\pi \times 85 \text{ Hz}. \end{aligned}$$

The resulting dressed-state potential is given by [58]

$$\begin{aligned} V_\lambda &= g_F \mu_B \tilde{m}_F \sqrt{\left(\frac{\hbar \omega_{\text{RF}}}{|g_F| \mu_B} - |\mathbf{B}| \right)^2 + \left(\frac{B_{\text{RF}\perp}(t)}{2} \right)^2}, \\ &= g_F \mu_B \tilde{m}_F \sqrt{\Delta_{\text{RF}}(\mathbf{r})^2 + \Omega_{\text{rabi}}^2(t)} \end{aligned}$$

with $\tilde{m}_F = 2$, ω_{RF} the frequency of the RF radiation and $B_{\text{RF}\perp}$ denoting the component of the linear polarized dressing field \mathbf{B}_{RF} that is aligned perpendicular to the static field. As in [54] we use a detuning of $\Delta_{\text{RF}}(0) = -2\pi \times 30$ kHz from the $m_F = 2 \rightarrow m_F = 1$ transition for the simulation. The Rabi-frequency is parameterized by the control parameter λ

$$\Omega_{\text{rabi}}(\lambda) = \Omega_{\text{rabi}}^* \chi(\lambda), \quad \Omega_{\text{rabi}}^* = 2\pi \times 155 \text{ kHz}$$

wherein

$$\lambda_1(0) = 0, \quad \lambda_1(T) = 1.$$

The control parameter λ mimics the situation in experiments, where the double well potential is controlled by changing the RF field amplitude through an RF current in a wire. For $\lambda = 0$ we recover the static harmonic potential, whereas $\lambda = 1$ corresponds to a fully separated double well with no wave function overlap between the two halves of the system. Since the Rabi-frequency is strictly positive in experiments we employ the same saturation function χ as in the previous example (see figure 4).

As the trapping potential is significantly changed during the splitting the atoms are radially displaced from their equilibrium position in the harmonic trap. Consequently, strong dipole and breathing oscillations are usually observed in experiments. This poses a strong limitation to the use of such systems as interferometers [56]. The minimization of such excitations is therefore one of the main motivations for our optimization.

3.3.2. Numerical simulations: single-parameter control

We illustrate the splitting procedure for $N = 2000$ atoms and $T = 6$ ms.

In a first step we again consider the case where the Rabi-frequency is increased linearly (see figure 7(a)). This procedure is similar to the one that is typically used in experiments [49, 53]. At the final time $t = T$ the infidelity has only decreased slightly as can be seen from figure 7(b). Moreover, the infidelity shows the expected strong oscillations for $t > T$. A snapshot of the density at time $t^* = 22.5$ ms is illustrated in figures 7(c)–(e), revealing that there is a large discrepancy between the computed state ψ and the desired state ψ_d .

Next, we consider the result of the optimal control algorithm. We find that, irrespective of the specific choice of the initial guess λ^0 , the algorithm always converges to approximately the same minimizer of the cost functional. The corresponding time-evolution of the Rabi-frequency is shown in figure 7(f). We observe that the Rabi-frequency remains zero for the first few milliseconds. In fact, only about three milliseconds of the optimization time T are used for the transformation of the external potential. This behavior persists even if we increase the optimization time T , with the Rabi-frequency vanishing for an even longer initial period of time. The precise timescale depends on the parameters of the trap, as the optimization algorithm tries to find a compromise between longitudinal and radial directions.

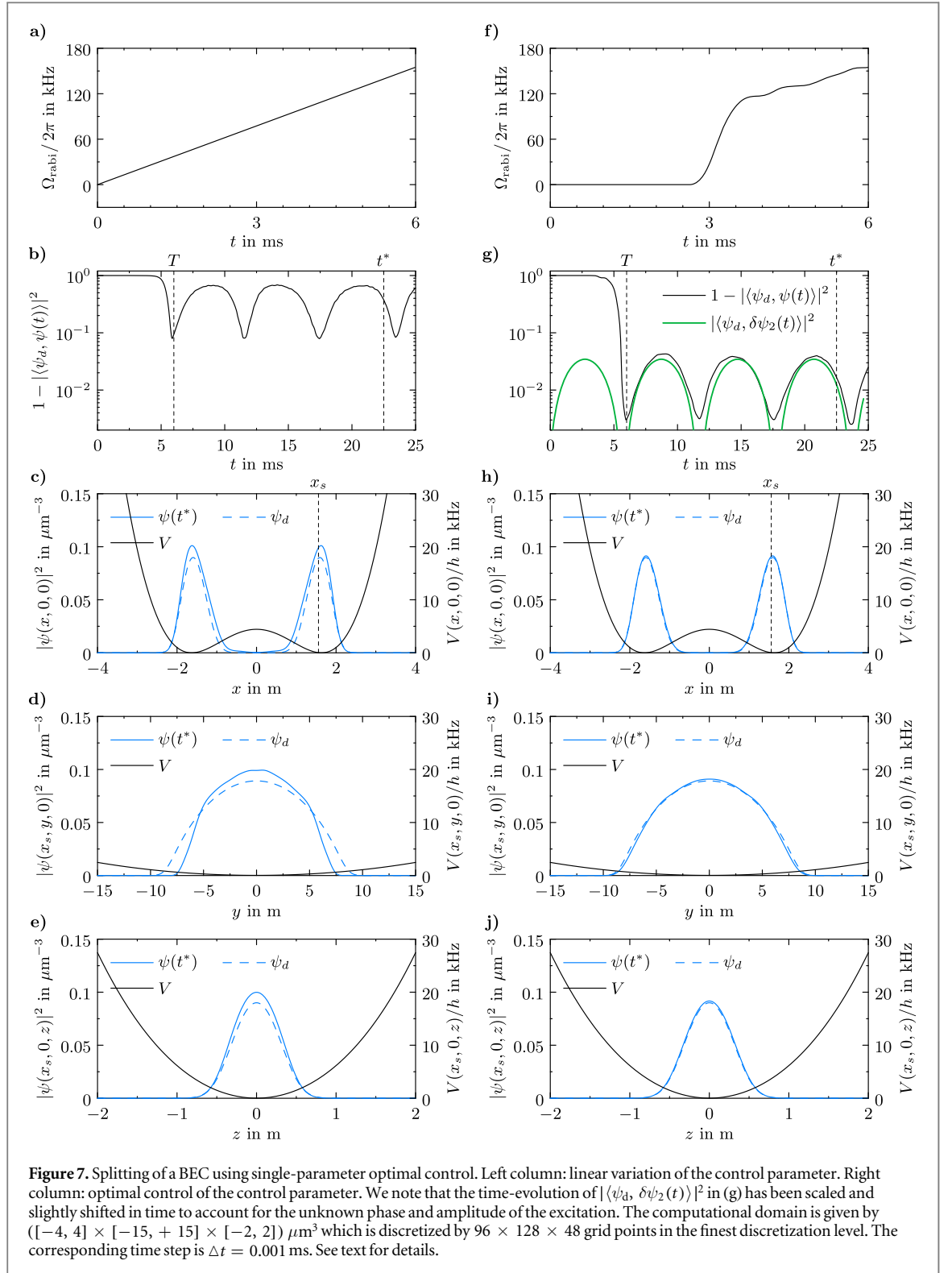
Interestingly, our 3D control qualitatively resembles the result of a previous 1D optimization that included beyond mean-field effects to model the distribution of atoms into the two final gases on the quantum level [57]. In both cases, the initial BEC is first rapidly split into two halves. Subsequently, these two halves are kept close enough to experience a tunnel coupling for a finite time-scale. This qualitative observation is very interesting, as reducing relative number fluctuations can help to significantly enhance the sensitivity of such interferometers. A detailed study of how useful our control can be in this context will be a natural extension of this work.

As a result of the optimal control algorithm the infidelity at the final time T is reduced by more than two orders of magnitude (see figure 7(g)). However, for $t > T$ we again observe a strong oscillation. Snapshots of the density distribution at $t^* = 22.5$ ms are given in figures 7(h)–(j).

3.3.3. Bogoliubov–de Gennes analysis

Interestingly, the 6 ms period of the very regular infidelity oscillation shown in figure 7(g) for the optimized splitting is approximately the same as the period of the infidelity oscillation depicted in figure 7(b) for the simple linear splitting. This suggests that the character of the oscillation is determined by the intrinsic properties of the BEC rather than by the splitting protocol.

Indeed, we demonstrate in the following that the oscillations are caused by collective excitations of the BEC, which are created during, but irrespective of the details of the splitting process. To this end, we show that they are



the result of a small deviation $\delta\psi$ from the desired state ψ_d , which can be described within the Bogoliubov–de Gennes (BdG) framework.

Let therefore $\Phi(\mathbf{r}, t) = \phi(\mathbf{r})e^{-i\mu t/\hbar}$ denote an eigenstate solution of the GPE. Here, μ is the corresponding chemical potential and ϕ is a solution of the stationary GPE, $H_0\phi + g|\phi|^2\phi = \mu\phi$, with $H_0 = -\hbar^2/2m\Delta + V$. We consider a generic state ψ which deviates from the eigenstate solution by a small fluctuation $\delta\psi$, i.e.,

$$\psi(\mathbf{r}, t) \approx \Phi(\mathbf{r}, t) + \delta\psi(\mathbf{r}, t). \quad (13)$$

In a linear approximation (with respect to $\delta\psi$) this small deviation is given by

$$\delta\psi(\mathbf{r}, t) = \left(u(\mathbf{r})e^{-i\omega t} + v^*(\mathbf{r})e^{i\omega^*t} \right) e^{-i\mu t/\hbar}, \quad (14)$$

where u , v and ω are defined via the solutions of the BdG equations [59, 60]

$$\begin{bmatrix} H_0 - \mu + 2g|\phi|^2 & g\phi^2 \\ - (g\phi^2)^* & -H_0 + \mu - 2g|\phi|^2 \end{bmatrix} \begin{bmatrix} u \\ v \end{bmatrix} = \hbar\omega \begin{bmatrix} u \\ v \end{bmatrix}. \quad (15)$$

We want to investigate small fluctuations $\delta\psi$ corresponding to some of the lowest energy eigenvalues $\hbar\omega$ in equation (15). To this end, we proceed in a conceptually similar way to [61] where numerical methods are used to investigate the stability and decay rates of non-isotropic attractive BECs. Like in [61] we consider the full 3D problem. However, for the discretization of the operators in (15) we employ a high-order finite difference discretization rather than working in a Fourier basis. By gradually increasing the spatial resolution of the finite difference discretization we are able to verify the convergence of the algorithm. A detailed description of our implementation is again given in the appendix.

As an example, we find that the first three eigenvalues converge towards $\omega_1 = \pm 314.54$ Hz, $\omega_2 = \pm 523.49$ Hz and $\omega_3 = \pm 734.26$ Hz. Subsequently, the corresponding eigenfunctions (u_i , v_i) are normalized according to the norm [60]

$$\int_{\mathbb{R}^3} (u_i^2(\mathbf{r}) - v_i^2(\mathbf{r})) d\mathbf{r} = 1. \quad (16)$$

Knowing the frequencies ω_i and amplitude functions u_i and v_i , it is possible to investigate the time-evolution of the excitations given by equation (14). It turns out that $|\delta\psi_i(t)|^2$ can be well described by a simple periodic oscillation in amplitude, while the shape remains mostly unchanged (see left column in figure 8). As u_i and v_i are purely real-valued functions, which approximately fulfill $v_i = -u_i$ (see right column in figure 8) we find $\delta\psi_i(\mathbf{r}, T_i/2) \approx \delta\psi_i(\mathbf{r}, T_i)$ and hence the effective oscillation periods are halved with respect to the eigenvalues found above, i.e. $T_{\text{eff},i} = T_i/2 = \pi/\omega_i$. In detail we find $T_{\text{eff},1} = 9.99$ ms, $T_{\text{eff},2} = 6.00$ ms and $T_{\text{eff},3} = 4.28$ ms.

Note that the effective period of the second excitation is very close to the period of the oscillation of the infidelity observed above. Indeed, plotting the time-evolution of $|\langle \psi_d, \delta\psi_2(t) \rangle|^2$ along with the time-evolution of the infidelity in figure 7(g) demonstrates clearly that the oscillation of the infidelity is dominated by the second excitation. As further evidence, we extract the deviation of ψ from ψ_d from our simulation. A comparison shows again very good agreement with the time-evolution of $\delta\psi_2(t)$ (see the appendix).

The fact that only the second but not the first excitation contributes to the observations can be understood from symmetry arguments. The first excitation corresponds to an antisymmetric wave function with respect to the longitudinal direction, whereas the second excitation is symmetric. During the splitting process, the halving of the atom number in each of the two gases, as well as an overall change in the longitudinal trapping potential leads to a symmetric change in the extension of the BEC in this direction. If the control is unable to compensate for this change in extension, the second Bogoliubov–de Gennes mode is automatically excited.

This effect is especially pronounced for the linear splitting. In contrast to that, the optimal control algorithm can still reduce the infidelity at $t = T$, but even a small deviation of the wave function from the stationary state leads to a strong oscillation in the infidelity for $t \geq T$.

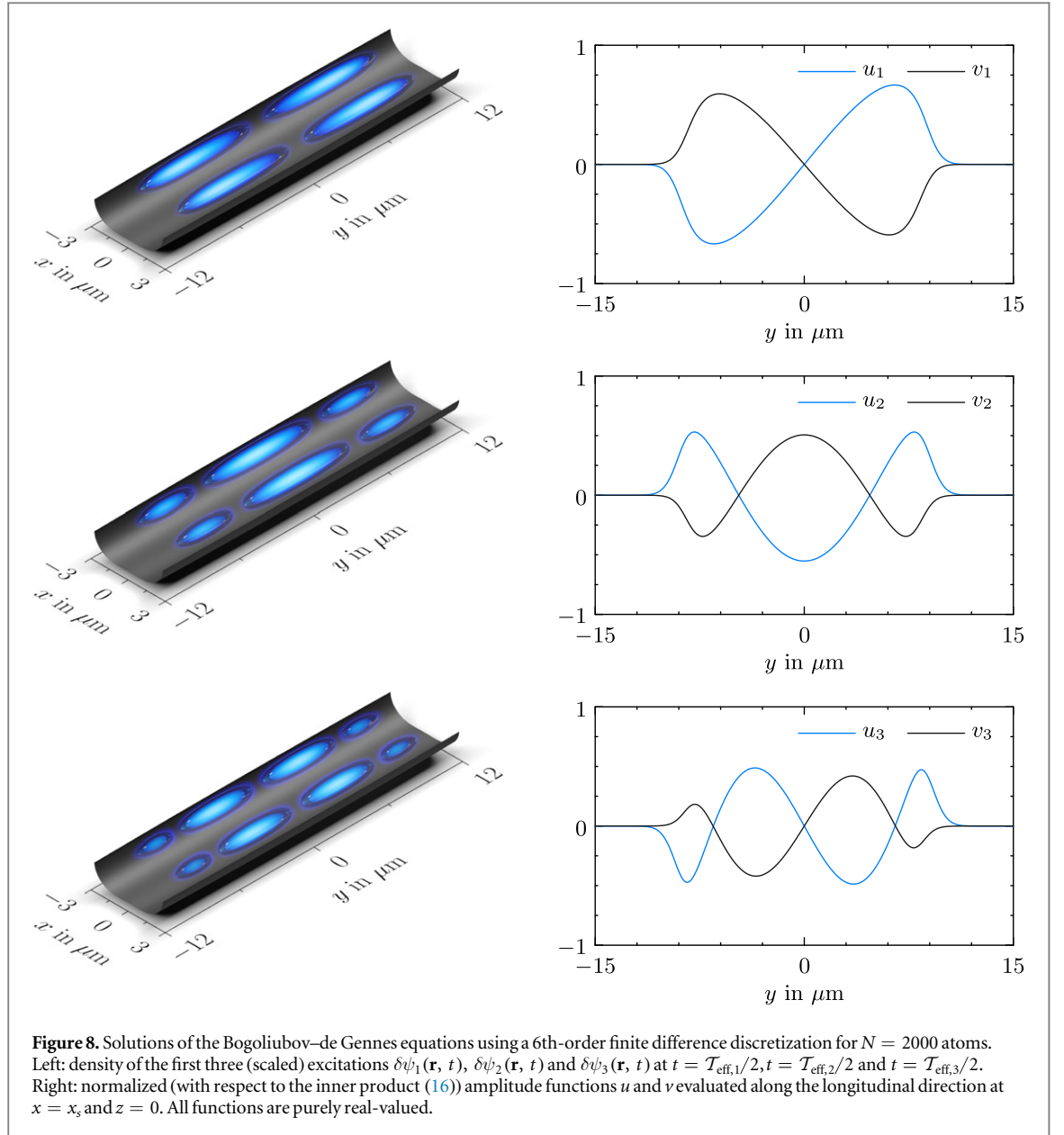
Once the wave function differs from the stationary state in the longitudinal direction it is impossible to stop the observed oscillation by a simple variation of the Rabi-frequency. The BEC will thus oscillate for $t > T$ after the end of the control.

A central role in this scenario is played by the longitudinal frequency ω_y . The smaller ω_y , the longer the extension of the condensate in the longitudinal direction. In analogy to a classical harmonic oscillator this increases the susceptibility to small deviations from the equilibrium position. We have confirmed this intuition with additional simulations, finding an even more pronounced excitation of the second mode for smaller ω_y .

This is particularly noteworthy with respect to experiments studying BECs in the 1D limit, where $\omega_{x,z} \gg \omega_y$ [53]. Intuitively, such experiments should be very well described through a 1D approximation, where only a reduced GPE for the x -direction has to be considered (see the appendix). Our results here show that such an approach will, in general, also lead to a strong breathing oscillation. Even if the 1D control is able to reach the 1D desired state with high precision, it does not necessarily describe the experimental reality and will thus fail in 3D.

3.3.4. Numerical simulations: two-parameter control

In the last part of this article we will show how the oscillations reported above can be eliminated using a more sophisticated control scheme that is made possible by the 3D character of our control and that involves a manipulation of the trapping potential along the longitudinal direction. In experiments on atom chips, this



manipulation can, for example, be realized using additional wire structures, which provide longitudinal confinement independent of the main radial trapping structures [62].

In analogy to the previous examples, we consider the following parameterization of Ω_{rabi} and ω_y :

$$\Omega_{\text{rabi}}(\lambda_1) = \Omega_{\text{rabi}}^* \chi(\lambda_1), \quad \Omega_{\text{rabi}}^* = 2\pi \times 155 \text{ kHz}, \quad (17a)$$

$$\omega_y(\lambda_2) = \omega_y^* \lambda_2, \quad \omega_y^* = 2\pi \times 85 \text{ Hz}, \quad (17b)$$

with

$$\begin{aligned} \lambda_1(0) &= 0, & \lambda_1(T) &= 1, \\ \lambda_2(0) &= 1, & \lambda_2(T) &= 1. \end{aligned}$$

The only difference to the previous example is thus that the value of the longitudinal trap frequency ω_y is now part of the control. We still fix $\omega_y(t=0) = 2\pi \times 85 \text{ Hz}$ and $\omega_y(t=T) = 2\pi \times 85 \text{ Hz}$ such that the initial and desired final states remain unchanged.

Using $\mathcal{X}^0(t) = [t/T, 1]$ for $t \in [0, T]$ as an initial guess the optimization algorithm converges to a solution which reduces the cost functional by more than three orders of magnitude. The time-evolution of the corresponding physical parameters is given in figure 9(a). As can be seen from figure 9(b) the infidelity remains very low for $t \geq T$. Snapshots of the density distribution at time $t^* = 22.5 \text{ ms}$ confirm that the deviation from the desired state is extremely small, see figures 9(d)–(f).

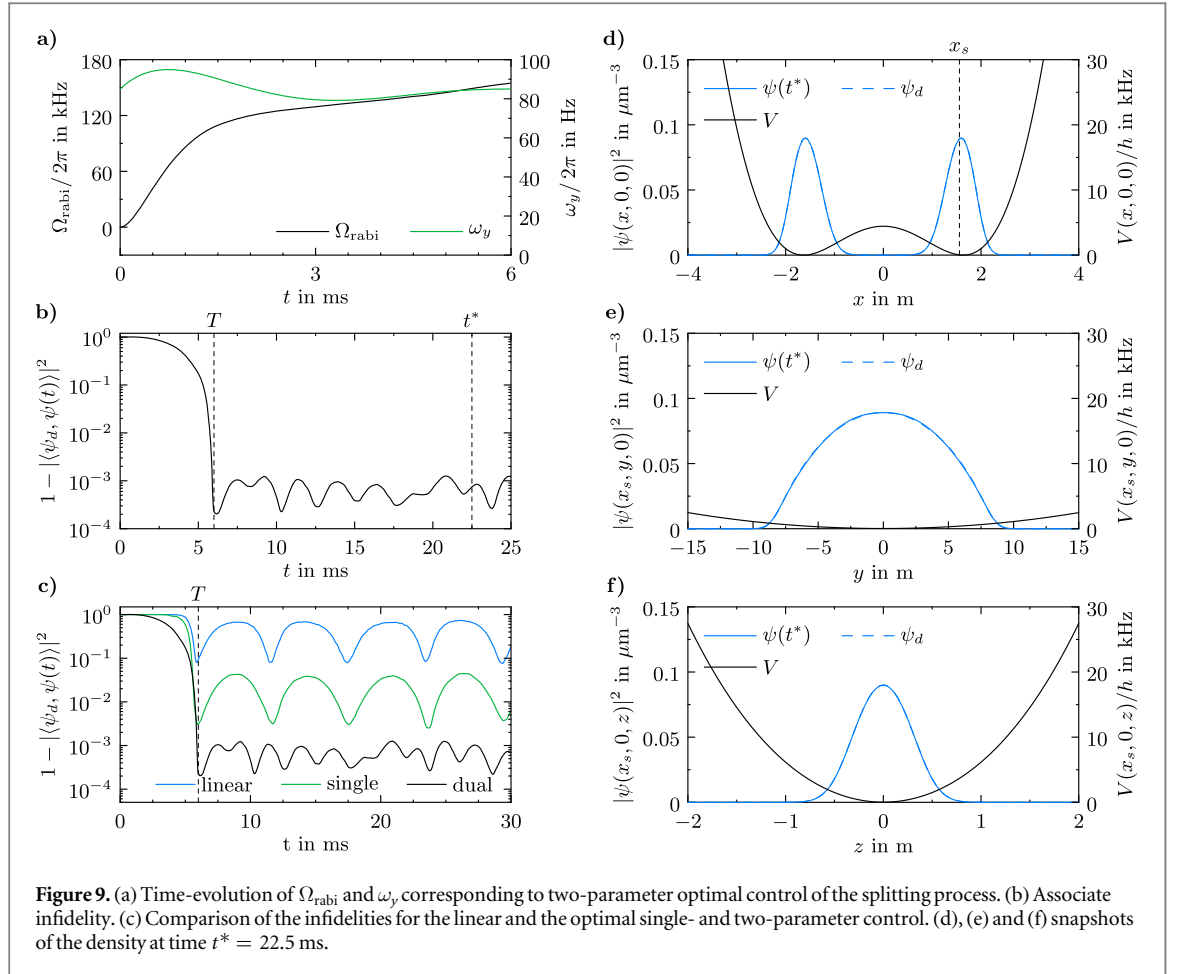


Figure 9. (a) Time-evolution of Ω_{rabi} and ω_y , corresponding to two-parameter optimal control of the splitting process. (b) Associate infidelity. (c) Comparison of the infidelities for the linear and the optimal single- and two-parameter control. (d), (e) and (f) snapshots of the density at time $t^* = 22.5$ ms.

In the given example we have chosen $T = \mathcal{T}_{\text{eff},2}$. In contrast to that, for a time $T < \mathcal{T}_{\text{eff},2}$ we find significantly worse results. The minimum time scale T is thus set by the oscillation period of the excitation that the control aims to stop. This oscillation period is in turn set by the geometry of the trap. Each different experimental situation will thus require carefully chosen parameters for the control.

4. Conclusion and outlook

In this work we have presented the first optimal control of the GPE in 3D. As we have shown, this situation is inherently more difficult than the optimal control of the 1D GPE because of the nonlinear coupling of different coordinate directions. We have performed a detailed analysis of the resulting small excitations, which we were able to minimize by extending previous control schemes from a single to a multi-parameter control.

In contrast to 1D approximations our 3D approach allows the study of realistic potentials. This will have direct impact on the quality of experiments and will therefore provide an important step in the ongoing effort to use the properties of the quantum world for real life applications. Importantly, our scheme is not limited to the examples discussed in this work but rather very flexible, with many more applications conceivable.

A straight-forward extension of our numerical solver could include the treatment of excited states. This would allow the 3D study of a recent experiment, where the BEC was transferred to the first excited state of the trapping potential via a 1D optimal control sequence [24]. Based on our observations we expect an even stronger excitation of BdG-modes in such an experiment. In that context, another interesting application would be to replace the cigar-shaped confinement potentials used in the splitting and vibrational state inversion experiments by torus-shaped trapping potentials. Due to the different topology the issues related to the excitation of small perturbations are expected to be strongly reduced.

Another obvious extension of this work could be to consider different cost functionals. More precisely, it would be interesting to investigate whether it is possible to reduce the optimization times T by using other cost functionals which are not based on the infidelity but rather on a conserved quantity like the total energy.

Finally, interesting further directions include the study of beyond mean-field effects using the multi-configurational time-dependent Hartree framework for bosons [63] or the optimization of finite temperature states.

Acknowledgments

We thank Jörg Schmiedmayer, Wolfgang Rohringer and Alexander Pikovski for helpful discussions. RML is supported by the Hertha-Firnberg Program of the Austrian Science Fund (FWF), Grant T402-N13. DM acknowledges Deutsche Forschungsgemeinschaft Collaborative Research Center TRR 109, Discretization in Geometry and Dynamics. TL acknowledges support by the FWF through the Doctoral Programme CoQuS (W1210) and by the Alexander von Humboldt Foundation through a Feodor Lynen Research Fellowship.

Appendix

A.1. Gradient of the reduced cost functional

In the main text we have introduced the cost functional $J(\boldsymbol{\lambda}, \psi)$ in (3) and the reduced cost functional $\hat{J}(\boldsymbol{\lambda}) = J(\boldsymbol{\lambda}, \psi_\lambda)$ in (7). Recall that, for a given control $\boldsymbol{\lambda} : (0, T) \rightarrow \mathbb{R}^m$ satisfying the boundary conditions (6c), ψ_λ is the solution to the initial value problem (5a) and (6a) for the GPE with the corresponding potential V_λ . Below, we argue why the H^1 -gradient of \hat{J} is given by the component $\boldsymbol{\Lambda} : (0, T) \rightarrow \mathbb{R}^m$ of the solution $(\psi, p, \boldsymbol{\Lambda})$ to the system consisting of (5a), (5b) and

$$\frac{d^2}{dt^2}(\boldsymbol{\Lambda} - \gamma\boldsymbol{\lambda}) = \text{Re} \left\langle p, \left(\partial_\lambda V_\lambda \right) \psi \right\rangle, \quad (18)$$

subject to the initial and terminal conditions (6a), (6b) and

$$\boldsymbol{\Lambda}(0) = \boldsymbol{\Lambda}(T) = 0. \quad (19)$$

Before discussing the gradient, we first calculate the variational derivative of \hat{J} . As it is customary in the context of optimization problems, we express the validity of the GPE (5a) in the form of a constraint $Z = 0$, with the constraint functional

$$Z(\boldsymbol{\lambda}, \psi) = i\partial_t \psi + \frac{1}{2}\Delta\psi - V_\lambda\psi - g|\psi|^2\psi.$$

By definition, ψ_λ satisfies $Z(\boldsymbol{\lambda}, \psi_\lambda) = 0$, hence

$$\hat{J}(\boldsymbol{\lambda}) = L(\boldsymbol{\lambda}, \psi_\lambda, p), \quad (20)$$

where L denotes the Lagrangian which was defined in equation (4) of the main text.

$$L(\boldsymbol{\lambda}, \psi, p) = J(\boldsymbol{\lambda}, \psi) + \text{Re} \int_0^T \langle p, Z(\boldsymbol{\lambda}, \psi) \rangle dt.$$

Equation (20) holds for arbitrary smooth functions $p : (0, T) \rightarrow L^2(\mathbb{R}^3; \mathbb{C})$. For fixed p , differentiation of \hat{J} in the direction $\delta\boldsymbol{\lambda}$ yields

$$\begin{aligned} D_\lambda \hat{J}(\boldsymbol{\lambda})[\delta\boldsymbol{\lambda}] &= D_\lambda L(\boldsymbol{\lambda}, \psi_\lambda, p)[\delta\boldsymbol{\lambda}] + D_\psi L(\boldsymbol{\lambda}, \psi_\lambda, p)[\delta\psi], \\ &= D_\lambda J(\boldsymbol{\lambda}, \psi_\lambda)[\delta\boldsymbol{\lambda}] + \text{Re} \int_0^T \langle p, D_\lambda Z(\boldsymbol{\lambda}, \psi_\lambda)[\delta\boldsymbol{\lambda}] \rangle dt, \\ &\quad + D_\psi J(\boldsymbol{\lambda}, \psi_\lambda)[\delta\psi] + \text{Re} \int_0^T \langle p, D_\psi Z(\boldsymbol{\lambda}, \psi_\lambda)[\delta\psi] \rangle dt, \end{aligned} \quad (21)$$

where $\delta\psi$ is the variation in ψ_λ induced by the variation $\delta\boldsymbol{\lambda}$ of $\boldsymbol{\lambda}$, i.e., it satisfies $D_\lambda Z(\boldsymbol{\lambda}, \psi_\lambda)[\delta\boldsymbol{\lambda}] + D_\psi Z(\boldsymbol{\lambda}, \psi_\lambda)[\delta\psi] = 0$ and $\delta\psi(0) = 0$. For simplification of $D_\lambda \hat{J}$, we choose p , which has been arbitrary up to this point, such that the last two terms in (21) cancel. Indeed, taking p as a solution to the terminal value problem (5b) and (6b), it follows that

$$\begin{aligned}
& D_\psi J(\boldsymbol{\lambda}, \psi_\lambda)[\delta\psi] + \operatorname{Re} \int_0^T \left\langle p, D_\psi Z(\boldsymbol{\lambda}, \psi_\lambda)[\delta\psi] \right\rangle dt, \\
& = -\operatorname{Re} \left(\left\langle \psi_d, \psi_\lambda(T) \right\rangle^* \left\langle \psi_d, \delta\psi(T) \right\rangle \right), \\
& + \operatorname{Re} \int_0^T \left\langle p, i\partial_t \delta\psi + \frac{1}{2} \Delta \delta\psi - V_\lambda \delta\psi - 2g |\psi_\lambda|^2 \delta\psi - g\psi_\lambda^2 \delta\psi^* \right\rangle dt, \\
& = \operatorname{Re} \int_0^T \left\langle i\partial_t p + \frac{1}{2} \Delta p - V_\lambda p - 2g |\psi_\lambda|^2 p - g\psi_\lambda^2 p^*, \delta\psi \right\rangle dt = 0.
\end{aligned}$$

To arrive at this result, we have performed an integration by parts with respect to time, using the terminal condition (6b) and the fact that $\delta\psi(0) = 0$ thanks to the initial condition (6a). In view of these cancellations, equation (21) simplifies to

$$D_\lambda \hat{J}(\boldsymbol{\lambda})[\delta\boldsymbol{\lambda}] = \gamma \int_0^T \partial_t \boldsymbol{\lambda} \cdot \partial_t(\delta\boldsymbol{\lambda}) dt - \operatorname{Re} \int_0^T \left\langle p, \partial_\lambda V_\lambda \cdot (\delta\boldsymbol{\lambda}) \psi \right\rangle dt. \quad (22)$$

We are now in the position to calculate the H^1 -gradient of \hat{J} . Recall that the Sobolev space $H^1(0, T; \mathbb{R}^m)$ consists of all square integrable functions $\boldsymbol{\lambda} \in L^2(0, T; \mathbb{R}^m)$ that possess a weak derivative $\partial_t \boldsymbol{\lambda} \in L^2(0, T; \mathbb{R}^m)$. Functions $\boldsymbol{\lambda} \in H^1(0, T; \mathbb{R}^m)$ are actually Hölder continuous, and therefore, they have well-defined boundary values at $t = 0$ and $t = T$. It is natural to consider the reduced cost functional \hat{J} as defined on $H_*^1(0, T; \mathbb{R}^m)$, which is the affine subspace of functions $\boldsymbol{\lambda} \in H^1(0, T; \mathbb{R}^m)$ that satisfy the boundary conditions (6c). Indeed, any admissible control $\boldsymbol{\lambda}: (0, T) \rightarrow \mathbb{R}^m$ must produce a finite value in the penalty term in J , which implies that $\partial_t \boldsymbol{\lambda} \in L^2(0, T; \mathbb{R}^m)$. The tangent space to $H_*^1(0, T; \mathbb{R}^m)$, i.e., the space of possible variations $\delta\boldsymbol{\lambda}$, is the linear subspace $H_0^1(0, T; \mathbb{R}^m)$ of all functions $\boldsymbol{\Lambda} \in H^1(0, T; \mathbb{R}^m)$ with vanishing boundary values, $\boldsymbol{\Lambda}(0) = \boldsymbol{\Lambda}(T) = 0$. This is a Hilbert space with respect to the inner product

$$(\boldsymbol{\Lambda}_1, \boldsymbol{\Lambda}_2) := \int_0^T \partial_t \boldsymbol{\Lambda}_1(t) \cdot \partial_t \boldsymbol{\Lambda}_2(t) dt.$$

By definition, the gradient of \hat{J} with respect to the inner product (\cdot, \cdot) is the uniquely determined element $\boldsymbol{\Lambda} \in H_0^1(0, T; \mathbb{R}^m)$ such that $(\boldsymbol{\Lambda}, \delta\boldsymbol{\lambda}) = D_\lambda \hat{J}(\boldsymbol{\lambda})[\delta\boldsymbol{\lambda}]$ for all variations $\delta\boldsymbol{\lambda} \in H_0^1(0, T; \mathbb{R}^m)$. In view of (22), $\boldsymbol{\Lambda}$ satisfies

$$\begin{aligned}
& \int_0^T \partial_t(\boldsymbol{\Lambda} - \gamma\boldsymbol{\lambda}) \cdot \partial_t(\delta\boldsymbol{\lambda}) dt \\
& = - \int_0^T \operatorname{Re} \left\langle p, \partial_\lambda V_\lambda \psi \right\rangle \cdot (\delta\boldsymbol{\lambda}) dt \quad \text{for all variations } \delta\boldsymbol{\lambda} \in H_0^1(0, T; \mathbb{R}^m),
\end{aligned} \quad (23)$$

and $\boldsymbol{\Lambda} \in H_0^1(0, T; \mathbb{R}^m)$ induces the boundary conditions (19). To verify that the solution $\boldsymbol{\Lambda}$ to the boundary value problem (18) and (19) satisfies (23), it suffices to integrate by parts in the time integral on the left-hand side, using that $\delta\boldsymbol{\lambda}(0) = \delta\boldsymbol{\lambda}(T) = 0$.

A.2. Algorithms and implementation

A.2.1. Numerical evaluation of the cost functional. The evaluation of the reduced cost functional (7) for a given control curve $\boldsymbol{\lambda}$ implicitly involves the computation of ψ_λ , that is, the solution of the GPE. No analytical solutions are available in general, so we use a numerical approximation. For brevity of notation, we write ψ instead of ψ_λ in the following.

For the numerical computation of the first term in (3), that is $1/2(1 - |\langle \psi_d, \psi(T) \rangle|^2)$, we have to solve the GPE (5a) with initial data (6a) for $t \in [0, T]$. Our simulations are performed on the spatial domain

$$\Omega = \left[-L_x/2, L_x/2 \right] \times \left[-L_y/2, L_y/2 \right] \times \left[-L_z/2, L_z/2 \right]$$

with L_x, L_y and L_z chosen sufficiently large to capture the significant part of the rapidly decaying solution ψ .

For numerical discretization in time, we employ the following time-splitting spectral method [32]:

$$\psi(t_{n+1}) \approx e^{-iB_n^+ \Delta t/2} e^{-iA \Delta t} e^{-iB_n^- \Delta t/2} \psi(t_n), \quad (24)$$

with operators $A = -1/2\Delta$, $B^\pm = V_{\chi^{(n+1/2)}} + g|\psi_n^\pm|^2$, and with $t_n = n\Delta t$, $n = 0, \dots, N-1$ such that $N\Delta t = T$. Here $\chi^{(n+1/2)} = 1/2(\boldsymbol{\lambda}(t_n) + \boldsymbol{\lambda}(t_{n+1}))$, and the choice of ψ_n^\pm is given below. Thus, the n th time step consists of the following three sub-steps. First, solve $i\partial_t \psi = (V_{\chi^{(n+1/2)}} + g|\psi(t_n)|^2)\psi$ for a duration of $\Delta t/2$ with initial value $\psi(t_n)$; thus $\psi_n^- = \psi(t_n)$. The result is used as initial value for the free Schrödinger equation $i\partial_t \psi = -1/2\Delta\psi$, which is then solved for duration of Δt ; the result is ψ_n^+ . Finally, $i\partial_t \psi = (V_{\chi^{(n+1/2)}} + g|\psi_n^+|^2)\psi$ is solved with initial value ψ_n^+ , again for a duration of $\Delta t/2$. The result of the third sub-step is taken as $\psi(t_{n+1})$.

The free Schrödinger equation is solved using the Fourier spectral method. To this end, the wave function ψ is interpolated by a trigonometric polynomial on the grid points of the cartesian grid

$$(x_{j_x}, y_{j_y}, z_{j_z}) = (-L_x/2 + j_x \Delta x, -L_y/2 + j_y \Delta y, -L_z/2 + j_z \Delta z),$$

where $\Delta x = L_x/J_x$ with $j_x = 0, \dots, J_x - 1$ etc. Thus, at time t_n , the wave function $\psi(t_n)$ is represented by a 3D array of complex numbers $\psi^{(n)} \in \mathbb{C}^{J_x J_y J_z}$.

As Matlab code, the n th time step looks as follows:

$$\begin{aligned} \psi &= \exp(-1i * (\mathbf{V}_{\lambda^{(n+1/2)}} + g * \text{abs}(\psi).^2) * \Delta t / 2) . * \psi; \\ \psi &= \text{fft}(\psi); \\ \psi &= \mathbf{M} . * \psi; \\ \psi &= \text{ifft}(\psi); \\ \psi &= \exp(-1i * (\mathbf{V}_{\lambda^{(n+1/2)}} + g * \text{abs}(\psi).^2) * \Delta t / 2) . * \psi; \end{aligned} \quad (25)$$

The array \mathbf{M} represents the action of the free Schrödinger operator. Due to the vectorized implementation in Matlab this procedure is highly efficient.

The method is of second order in time and of spectral accuracy in space, provided that ψ_0 and V_λ are sufficiently smooth. In comparison to a finite difference Crank–Nicolson scheme (see for example [21, 32]), the solution of a linear evolution equation is avoided, and less grid points $J = J_x J_y J_z$ are needed to achieve the same quality of approximation for ψ .

Typically, the numerical costs for our implementation (25) are dominated by the fast Fourier transforms `fft` and `ifft`, which are of order $\mathcal{O}(J \log J)$. However, in some simulations (splitting), the costs for computing the external potential $V_{\lambda^{(n+1/2)}}$ exceed that of the Fourier transforms.

For the numerical solution of the optimization problem, on the order of 10 to 100 evaluations of the cost functional are needed. The respective solution of the time-dependent GPE is performed on the graphics processing unit (GPU) of a powerful graphics card. Thanks to the vectorized implementation (25), it suffices to initialize the arrays ψ and \mathbf{V} once at the beginning, using the Matlab command `gpuArray`. For handling the intermediate results or for calling the data in the memory of the main processor at the end of the computation we use the command `gather`. The trap potentials need to be updated in each time step. However, these calculations can be performed in a vectorized way on the GPU as well.

Finally, we compute $1/2(1 - |\langle \psi_a, \psi(T) \rangle|^2)$ with $\psi(T) \approx \psi^{(N)}$, using a quadrature formula. The integral $\frac{\gamma}{2} \int_0^T |\partial_t \lambda(t)|^2 dt$ is computed by a quadrature formula as well, using a finite difference formula of second order for the approximation of the time derivative $\partial_t \lambda$.

A.2.2. Numerical computation of the gradient. According to (11a), the H^1 -gradient $\hat{J}(\lambda)$ is obtained as solution to the second order problem

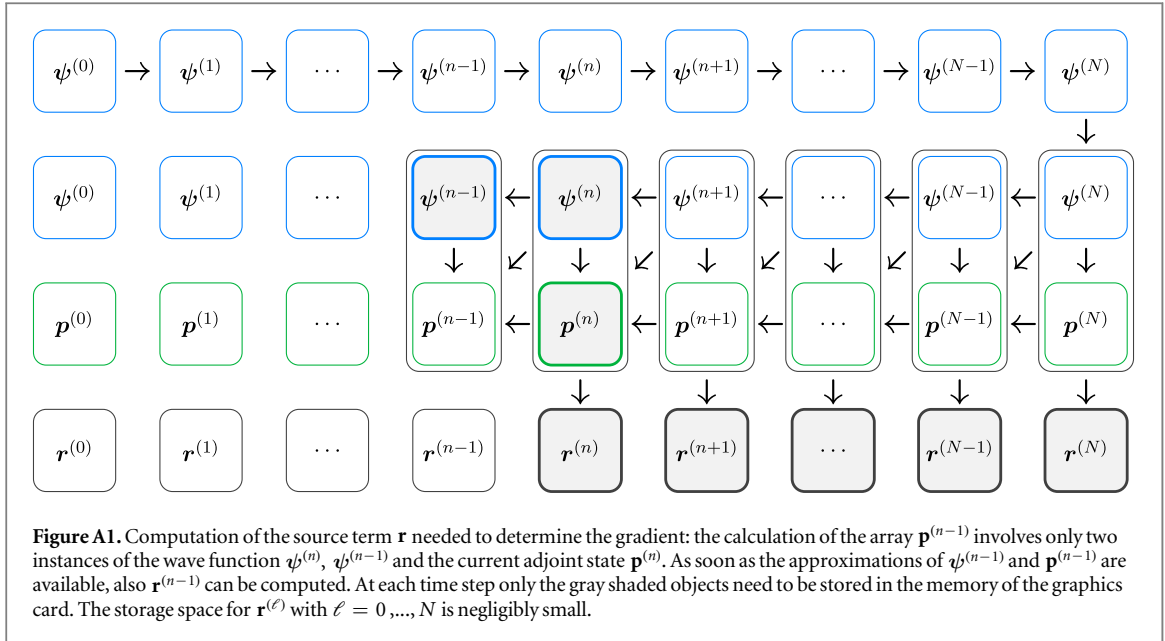
$$\frac{d^2}{dt^2} [\nabla \hat{J}(\lambda)] = \mathbf{r}(\lambda), \quad \mathbf{r}(\lambda) = \gamma \ddot{\lambda} + \text{Re} \left\langle \psi, \left(\partial_\lambda V_\lambda \right) p \right\rangle \quad (26)$$

subject to the boundary conditions $[\nabla \hat{J}(\lambda)](0) = \mathbf{0}$ and $[\nabla \hat{J}(\lambda)](T) = \mathbf{0}$. The time derivatives are discretized by second order finite differences.

To evaluate the right-hand side $\mathbf{r}(\lambda)$, the functions ψ and p need to be determined for $t \in [0, T]$. First, the state equation (5a) is solved as described above. Then, the adjoint equation (5b) is solved backwards in time, for the terminal condition (6b). For solution of the adjoint equation, a time-splitting method is applied as well: we alternately solve the equations $i\partial_t p = V_\lambda p + 2g|\psi|^2 p + g\psi^2 p^*$ and $i\partial_t p = -1/2\Delta p$. The free Schrödinger equation is discretized by the Fourier-spectral method, and the value of $\partial_\lambda V_\lambda$ at time $t = (n - 1/2)\Delta t$ is computed by means of the complex-step derivative approximation [64].

For integration of the adjoint equation on the time interval $[(n - 1)\Delta t, n\Delta t]$, an approximation of the wave function $\psi^{(n-1/2)} = 1/2(\psi^{(n-1)} + \psi^{(n)})$ is needed. Since it is impossible to store the arrays $\psi^{(n)}$ for every time step $n = 0, \dots, N$ on the graphics card, the state equation is simultaneously solved backwards in time as well. The procedure is sketched in figure A1: the calculation of $\mathbf{p}^{(n-1)}$ involves only two instances of the wave function and the ‘old’ adjoint state—that is, $\psi^{(n)}$, $\psi^{(n-1)}$, and $\mathbf{p}^{(n)}$. As soon as the approximations of $\psi^{(n-1)}$ and $\mathbf{p}^{(n-1)}$ are available, also $\mathbf{r}^{(n-1)}$ can be computed. In this way it is enough to store at each time step four arrays in 3D, and the values of all available $\mathbf{r}^{(n)}$ with $n = 0, \dots, N$ (the storage space of which is negligible).

A further difficulty in the numerical computation of the adjoint equation arises from the conjugate-complex quantity p^* in $g\psi^2 p^*$. Without going into details, we refer to the implementation in [27], which can be easily applied to the 3D case. As in the case of the GPE the computation of \mathbf{r} can be significantly accelerated by using



the graphics card. Still, the costs for the computation of the gradient are three to four times higher than for the evaluation of the cost functional.

A.2.3. Computation of the initial and desired final states. The initial and terminal states ψ_0 and ψ_d are assumed to be ground state solutions of the stationary GPE. We compute them by imaginary time propagation [65, 66] (also known as normalized gradient flow): the time step Δt in (25) is replaced by $-i\Delta t$, and the wave function ϕ is normalized after every time step. By using adaptive time stepping, we reach a sufficiently exact solution with justifiable numerical costs.

A.2.4. Further details of the implementation. For the numerical solution of the considered optimal control problems we use a personal computer (i7 – 4770K CPU @3.50 Ghz \times 8) and Matlab. The parts with the highest numerical costs, thus the solving of the partial differential equations and the computation of the external potentials, are performed on the graphics card (GeForce GTX TITAN), which accelerates the calculations significantly. The evaluation of the Fourier transform, for example, on the finest space discretization can be accelerated by a factor 4–6. In this context, it is important to mention that the CPU-version of `fft` in Matlab is parallelized as well and hence uses all cores available on the CPU.

In general it is useful to initially solve each optimal control problem with a small number of Fourier modes J_x, J_y, J_z and with a relatively big time step Δt . Subsequently, the same optimal control problem is solved on a finer mesh grid and with smaller time step, whereby as initial data λ^0 is used, obtained as approximated solution in the computation before. We repeat this procedure until the computed control curve with respect to the old discretization does not differ from the control curve of the finer discretization anymore.

We consider a sequence of discretization parameters

$$\begin{aligned} (J_x^{(1)}, J_y^{(1)}, J_z^{(1)}, (\Delta t)^{(1)}) &\rightarrow (J_x^{(2)}, J_y^{(2)}, J_z^{(2)}, (\Delta t)^{(2)}) \\ &\rightarrow \dots \rightarrow (J_x^{(M)}, J_y^{(M)}, J_z^{(M)}, (\Delta t)^{(M)}) \end{aligned}$$

with $J_x^{(\ell+1)} > J_x^{(\ell)}$, $J_y^{(\ell+1)} > J_y^{(\ell)}$, $J_z^{(\ell+1)} > J_z^{(\ell)}$ and $(\Delta t)^{(\ell+1)} < (\Delta t)^{(\ell)}$ for $\ell = 2, \dots, M$. Typically on the order of 10 to 100 iterations of the conjugate gradient method are needed for solving the optimal control problems on the coarse grid. The computational time is of some minutes. The numerical costs for the calculations of each single iteration increase rapidly with each discretization level. In the same time if one gets near to the local minimum, less iterations for finding the local minimum are required. By means of the described strategy each of the presented optimal control problems can be solved in several hours computing time with respect to the finest discretization level.

A.3. Numerical solution of the 3D Bogoliubov–de Gennes equations

For numerical treatment of (15), we proceed analogously to [67]: a change of variables $u = \frac{1}{2}(w_1 - w_2)$ and $v = \frac{1}{2}(w_1 + w_2)$ transforms the system into:

$$-\begin{bmatrix} H_0 - \mu + g\phi^2 \\ H_0 - \mu + 3g\phi^2 \end{bmatrix} \begin{bmatrix} w_1 \\ w_2 \end{bmatrix} = \hbar\omega \begin{bmatrix} w_1 \\ w_2 \end{bmatrix}. \quad (27)$$

A double application of the operator decouples the eigenvalue problem,

$$(H_0 - \mu + g\phi^2)(H_0 - \mu + 3g\phi^2)w_1 = \lambda w_1, \quad (28a)$$

$$(H_0 - \mu + 3g\phi^2)(H_0 - \mu + g\phi^2)w_2 = \lambda w_2, \quad (28b)$$

where $\lambda = \hbar^2\omega^2$. Clearly, it suffices to solve the first eigenvalue problem (28a).

The eigenvalue problem $Aw_1 = \lambda w_1$ given in (28a) can only be solved using numerical methods. To this end, the operator $A = (H_0 - \mu + g\phi^2)(H_0 - \mu + 3g\phi^2)$ is discretized via a 6th-order symmetric finite difference formula. Clearly, ϕ and μ need to be determined in advance and with high precision. Here, we solve

$$H_0\phi + g|\phi|^2\phi = \mu\phi, \quad H_0 = -\hbar^2/2m \Delta + V$$

using the same 6th-order finite difference discretization along with the imaginary time-stepping algorithm (see above). In this context, the second-order time-splitting method is replaced by the classical Runge–Kutta method of order 4. Subsequently, the chemical potential can be computed using the identity

$$\mu = \int_{\mathbb{R}^3} \left(\frac{1}{2} |\nabla\phi(\mathbf{r})|^2 + V(\mathbf{r}) |\phi(\mathbf{r})|^2 + g |\phi(\mathbf{r})|^4 \right) d\mathbf{r}.$$

Once ϕ and μ have been determined we need to solve the discretized eigenvalue problem (28a).

Naturally, we consider the same computational domain $([-4, 4] \times [-15, +15] \times [-2, 2]) \mu\text{m}^3$ that was used in the splitting experiment in section 3.3. Like in the original experiment we employ $J_x = 96$, $J_y = 128$ and $J_z = 48$ grid points in the respective coordinate directions (in the finest discretization level). The resulting large-scale eigenvalue problem is then solved efficiently by means of an iterative algorithm. For this purpose we employ the Matlab function `eigs` which only determines the most relevant eigenvalues and their corresponding eigenfunctions: the algorithm yields the eigenvalues closest to a specified shift σ which we set to a value slightly larger than zero. (We are only interested in the first few non-trivial solutions of (28a) corresponding to the eigenvalues of smallest magnitude.) The underlying algorithm of `eigs` requires the repeated solution of the linear system of equations

$$(A - \sigma I)x = b \quad (29)$$

for a given right-hand side b . We employ the biconjugate gradients stabilized method (`bicgstab`) which is implemented in Matlab as well. Note that $A - \sigma I$ is badly conditioned which is why the `bicgstab`-routine needs to be called with a preconditioner $M = M_1M_2$, i.e. equation (29) is effectively replaced by $M^{-1}(A - \sigma I)x = M^{-1}b$. We found that the algorithm converges reasonably fast when the factors M_1 and M_2 are given by the matrices L and U obtained from a sparse incomplete LU -factorization. Such an approximate factorization of $A - \sigma I$ can be computed using another Matlab function called `ilu`. For further information about the Matlab functions mentioned above we refer to the Matlab documentation and the literature cited therein. The time needed to compute a few eigenvalue-eigenvector solutions of the Bogoliubov–de Gennes equations depends strongly on the number of grid points J_x , J_y and J_z . For the number of grid points reported above the whole computation takes on the order of five hours computing time utilizing the above mentioned CPU.

A.4. Extracting the excitation from the time-evolution of the wave-function

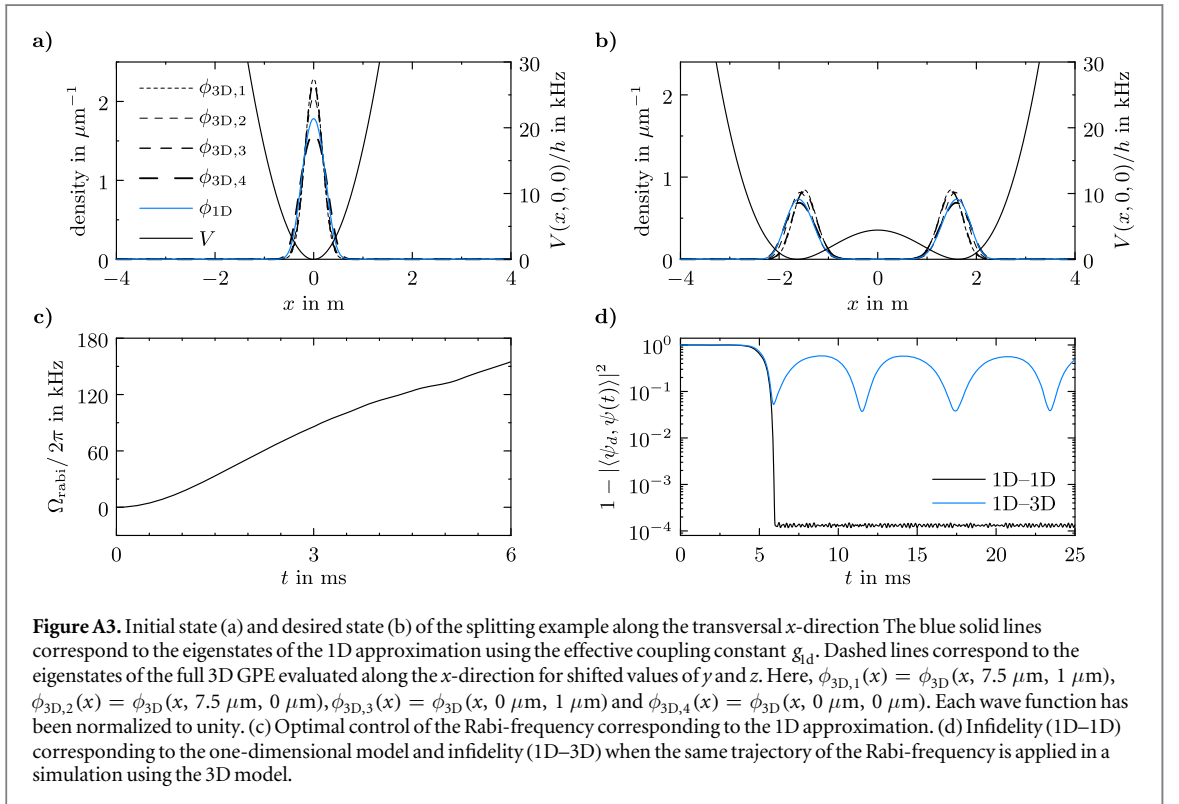
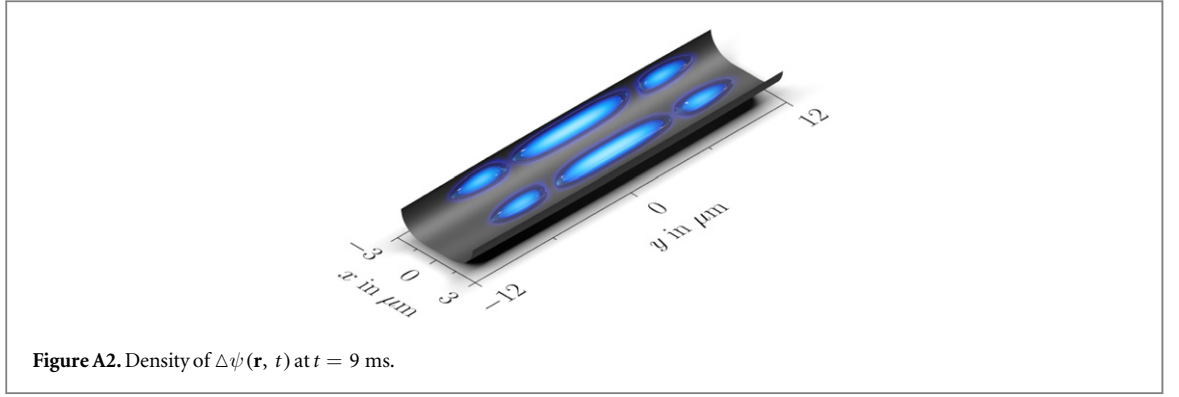
The small perturbation which causes the oscillation of the infidelity in the splitting example can be extracted directly from the time-evolution of the wave function ψ . To this end, we assume that $\psi(\mathbf{r}, t)$ and $\psi_d(\mathbf{r})$ are almost identical for $t = T$, i.e.,

$$\psi(t = T) \approx e^{i\theta}\psi_d, \quad \theta = \arg \min_{\theta'} \left\| \psi(T) - e^{i\theta'}\psi_d \right\|.$$

This assumption is in good agreement with our observations, where the minimum value of the infidelity is reached at this point in time. In analogy to equation (13) we define the difference $\Delta\psi := \psi(\mathbf{r}, t) - \Phi(\mathbf{r}, t)$, which leads to the result

$$\Delta\psi(\mathbf{r}, t) := \psi(\mathbf{r}, t) - e^{i\theta}\psi_d(\mathbf{r})e^{-i\mu(t-T)/\hbar}, \quad t \geq T.$$

Here, we have introduced an additional phase factor $e^{i\mu T/\hbar}$ in order to take into account that we consider the time-evolution of $\Delta\psi$ starting at $t = T$. A snapshot of the density $|\Delta\psi(\mathbf{r}, t)|^2$ for $t = 9$ ms is shown in figure A2. It is quite obvious that the distribution of the density is very similar to the distribution of the density of the second excitation depicted in figure 8.



A.5. 1D approximation for the splitting of a BEC

We briefly discuss the 1D approximation for the splitting example. In this case, the reduced GPE for the x -direction is given by

$$i\hbar \partial_t \psi = -\frac{\hbar^2}{2m} \partial_{xx} \psi + V_\lambda(x, 0, 0) \psi + g_{1d} |\psi|^2 \psi,$$

where the effective 1D interaction strength g_{1d} is found by integrating out the two transversal dimensions [68, 69]

$$g_{1d} \approx g \int_{-\infty}^{\infty} \int_{-\infty}^{\infty} |\tilde{\phi}(y, z)|^4 dy dz. \quad (30)$$

Here, $\tilde{\phi}(y, z) := \phi(0, y, z)$ corresponds to the normalized ground-state solution of the 3D model in the $(x \equiv 0)$ -plane.

With this approximation we find $g_{1d} \approx h \times 1300.44 \text{ Hz } \mu\text{m}$ for $N = 2000$ atoms. This value describes the situation along the whole x -axis and also leads to reasonable results away from the center of the cloud, as can be seen from figures A3 (a)–(b). We then follow the same procedures as in the 3D case to find an optimal control trajectory for the Rabi frequency.

References

- [1] Bloch I, Dalibard J and Zwerger W 2008 *Rev. Mod. Phys.* **80** 885

- [2] Gross C, Zibold T, Nicklas E, Esteve J and Oberthaler M K 2010 *Nature* **464** 1165
- [3] Lücke B et al 2011 *Science* **334** 773
- [4] Riedel M F, Böhi P, Li Y, Hänsch T W, Sinatra A and Treutlein P 2010 *Nature* **464** 1170
- [5] Ockeloen C F, Schmied R, Riedel M F and Treutlein P 2013 *Phys. Rev. Lett.* **111** 143001
- [6] Wildermuth S, Hofferberth S, Lesanovsky I, Haller E, Andersson L M, Groth S, Bar-Joseph I, Krüger P and Schmiedmayer J 2005 *Nature* **435** 440
- [7] Aigner S, Della Pietra L, Japha Y, Entin-Wohlman O, David T, Salem R, Folman R and Schmiedmayer J 2008 *Science* **319** 1226
- [8] Geiger R et al 2011 *Nat. Commun.* **2** 474
- [9] Bloom B, Nicholson T, Williams J, Campbell S, Bishop M, Zhang X, Zhang W, Bromley S and Ye J 2014 *Nature* **506** 71–5
- [10] Calarco T, Hinds E, Jaksch D, Schmiedmayer J, Cirac J and Zoller P 2000 *Phys. Rev. A* **61** 022304
- [11] Kielpinski D, Monroe C and Wineland D J 2002 *Nature* **417** 709
- [12] Bloch I, Dalibard J and Nascimbène S 2012 *Nat. Phys.* **8** 267
- [13] Peirce A P, Dahleh M A and Rabitz H 1988 *Phys. Rev. A* **37** 4950
- [14] Koch C P, Palao J P, Kosloff R and Masnou-Seeuws F 2004 *Phys. Rev. A* **70** 013402
- [15] Rabitz H, de Vivie-Riedle R, Motzkus M and Kompa K 2000 *Science* **288** 824
- [16] Borzi A, Stadler G and Hohenester U 2002 *Phys. Rev. A* **66** 053811
- [17] Hohenester U 2006 *Phys. Rev. B* **74** 161307
- [18] Nöbauer T, Angerer A, Bartels B, Trupke S, Rotter S, Schmiedmayer J, Mintert F and Majer J 2014 arXiv:1412.5051
- [19] Pethick C and Smith H 2002 *Bose–Einstein Condensation in Dilute Gases* (Cambridge: Cambridge University Press)
- [20] Dalfovo F, Giorgini S, Pitaevskii L P and Stringari S 1999 *Rev. Mod. Phys.* **71** 463
- [21] Hohenester U, Rekdal P K, Borzi A and Schmiedmayer J 2007 *Phys. Rev. A* **75** 023602
- [22] Peirce A P, Dahleh M A and Rabitz H 1988 *Phys. Rev. A* **37** 4950
- [23] Jäger G and Hohenester U 2013 *Phys. Rev. A* **88** 035601
- [24] Bücken R, Grond J, Manz S, Berrada T, Betz T, Koller C, Hohenester U, Schumm T, Perrin A and Schmiedmayer J 2011 *Nat. Phys.* **7** 608
- [25] van Frank S, Negretti A, Berrada T, Bücken R, Montangero S, Schaff J-F, Schumm T, Calarco T and Schmiedmayer J 2014 *Nat. Commun.* **5** 4009
- [26] Hohenester U 2014 *Comput. Phys. Commun.* **185** 194
- [27] von Winckel G and Borzi A 2008 *Inverse Problems* **24** 034007
- [28] Bücken R, Berrada T, van Frank S, Schaff J-F, Schumm T, Schmiedmayer J, Jäger G, Grond J and Hohenester U 2013 *J. Phys. B: At. Mol. Opt. Phys.* **46** 104012
- [29] Jäger G and Hohenester U 2013 *Phys. Rev. A* **88** 035601
- [30] Jäger G, Reich D M, Goerz M H, Koch C P and Hohenester U 2014 *Phys. Rev. A* **90** 033628
- [31] Hager W and Zhang H 2005 *SIAM J. Optim.* **16** 170
- [32] Bao W, Jaksch D and Markowich P A 2003 *J. Comput. Phys.* **187** 318
- [33] A three-dimensional visualization of the numerical examples considered in this article is available online (<https://www.youtube.com/watch?v=DEcnqSwPgrw>)
- [34] Ketterle W, Durfee D S and Stamper-Kurn D M 1999 *Proc. Int. Sch. Phys. “Enrico Fermi”* **140** 67–176
- [35] Schaff J-F, Song X-L, Capuzzi P, Vignolo P and Labeyrie G 2011 *Europhys. Lett.* **93** 23001
- [36] Masuda S, Nakamura K and del Campo A 2014 *Phys. Rev. Lett.* **113** 063003
- [37] Seaman B T, Krämer M, Anderson D Z and Holland M J 2007 *Phys. Rev. A* **75** 023615
- [38] Henderson K, Ryu C, MacCormick C and Boshier M 2009 *New J. Phys.* **11** 043030
- [39] Shvachuk I, Bugge C, Petrov D S, Dieckmann K, Zielonkowski M, Kemmann M, Tiecke T G, von Klitzing W, Shlyapnikov G V and Walraven J T M 2002 *Phys. Rev. Lett.* **89** 270404
- [40] Ryu C, Andersen M, Cladé P, Natarajan V, Helmerson K and Phillips W 2007 *Phys. Rev. Lett.* **99** 260401
- [41] Ryu C, Blackburn P W, Blinova A A and Boshier M G 2013 *Phys. Rev. Lett.* **111** 205301
- [42] Beattie S, Moulder S, Fletcher R J and Hadzibabic Z 2013 *Phys. Rev. Lett.* **110** 025301
- [43] Jendrzejewski F, Eckel S, Murray N, Lanier C, Edwards M, Lobb C J and Campbell G K 2014 *Phys. Rev. Lett.* **113** 045305
- [44] Eckel S, Lee J G, Jendrzejewski F, Murray N, Clark C W, Lobb C J, Phillips W D, Edwards M and Campbell G K 2014 *Nature* **506** 200
- [45] Lesanovsky I, Schumm T, Hofferberth S, Andersson L M, Krüger P and Schmiedmayer J 2006 *Phys. Rev. A* **73** 033619
- [46] Schumm T, Hofferberth S, Andersson L M, Wildermuth S, Groth S, Bar-Joseph I, Schmiedmayer J and Krüger P 2005 *Nat. Phys.* **1** 57
- [47] Folman R, Krüger P, Schmiedmayer J, Denschlag J and Henkel C 2002 *Adv. At. Mol. Opt. Phys.* **48** 263
- [48] Reichel J and Vuletic V 2010 *Atom Chips* (New York: Wiley)
- [49] Gring M, Kuhnert M, Langen T, Kitagawa T, Rauer B, Schreitl M, Mazets I, Smith D A, Demler E and Schmiedmayer J 2012 *Science* **337** 1318
- [50] Kuhnert M, Geiger R, Langen T, Gring M, Rauer B, Kitagawa T, Demler E, Adu Smith D and Schmiedmayer J 2013 *Phys. Rev. Lett.* **110** 090405
- [51] Smith D A, Gring M, Langen T, Kuhnert M, Rauer B, Geiger R, Kitagawa T, Mazets I, Demler E and Schmiedmayer J 2013 *New J. Phys.* **15** 075011
- [52] Langen T, Gring M, Kuhnert M, Rauer B, Geiger R, Smith D A, Mazets I E and Schmiedmayer J 2013 *Eur. Phys. J. Spec. Top.* **217** 43
- [53] Langen T, Erne S, Geiger R, Rauer B, Schweigler T, Kuhnert M, Rohringer W, Mazets I E, Gasenzer T and Schmiedmayer J 2014 *Science* **348** 207
- [54] Langen T, Geiger R, Kuhnert M, Rauer B and Schmiedmayer J 2013 *Nat. Phys.* **9** 640–3
- [55] Geiger R, Langen T, Mazets I and Schmiedmayer J 2014 *New J. Phys.* **16** 053034
- [56] Berrada T, van Frank S, Bücken R, Schumm T, Schaff J-F and Schmiedmayer J 2013 *Nat. Commun.* **4**
- [57] Grond J, von Winckel G, Schmiedmayer J and Hohenester U 2009 *Phys. Rev. A* **80** 053625
- [58] Lesanovsky I, Schumm T, Hofferberth S, Andersson L M, Krüger P and Schmiedmayer J 2006 *Phys. Rev. A* **73** 033619
- [59] Leggett A J 2001 *Rev. Mod. Phys.* **73** 307
- [60] Takahashi J, Nakamura Y and Yamanaka Y 2014 *Ann. Phys., NY* **347** 250
- [61] Huepe C, Tuckerman L, Métens S and Brachet M 2003 *Phys. Rev. A* **68** 023609
- [62] Langen T 2013 *PhD Thesis* Technische Universität Wien
- [63] Meyer H-D, Manthe U and Cederbaum L S 1990 *Chem. Phys. Lett.* **165** 73
- [64] Squire W and Trapp G 1998 *SIAM Rev.* **40** 110
- [65] Chiofalo M L, Succi S and Tosi M P 2000 *Phys. Rev. E* **62** 7438

- [66] Bao W and Du Q 2004 *SIAM J. Sci. Comput.* **25** 1674
- [67] Ronen S, Bortolotti D and Bohn J 2006 *Phys. Rev. A* **74** 013623
- [68] Salasnich L, Parola A and Reatto L 2002 *Phys. Rev. A* **65** 043614
- [69] Olshanii M 1998 *Phys. Rev. Lett.* **81** 938